Article

A Co-Doped Nanorod-like RuO$_2$ Electrocatalyst with Abundant Oxygen Vacancies for Acidic Water Oxidation

Oxygen
vacancy

Yuanyuan Tian, Shuo Wang, Ever Velasco, ..., Yichao Lin, Qiuju Zhang, Liang Chen

yclin@nimte.ac.cn (Y.L.)
zhangqj@nimte.ac.cn (Q.Z.)
chenliang@nimte.ac.cn (L.C.)

HIGHLIGHTS

A Co-doped RuO$_2$ electrocatalyst with an abundance of oxygen vacancies was synthesized

The compound exhibits ultra-high OER performance in acidic media

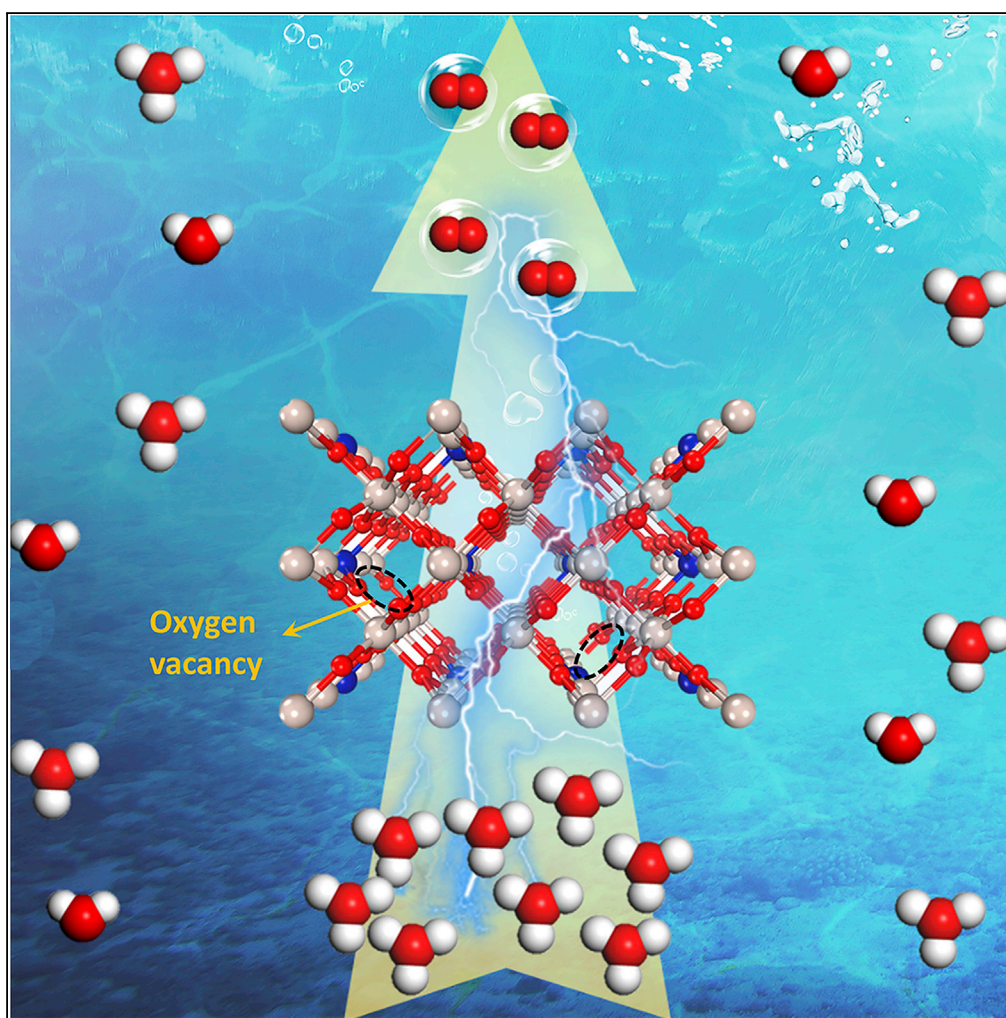The oxygen vacancies contribute to the high OER performance

Article

A Co-Doped Nanorod-like RuO$_2$ Electrocatalyst with Abundant Oxygen Vacancies for Acidic Water Oxidation

Yuanyuan Tian,[1,3,8] Shuo Wang,[1,8] Ever Velasco,[4] Yueping Yang,[5] Lujie Cao,[6] Linjuan Zhang,[7] Xing Li,[3] Yichao Lin,[1,2,*] Qiuju Zhang,[1,2,*] and Liang Chen[1,2,9,*]

SUMMARY

Active and highly stable electrocatalysts for oxygen evolution reaction (OER) in acidic media are currently in high demand as a cleaner alternative to the combustion of fossil fuels. Herein, we report a Co-doped nanorod-like RuO$_2$ electrocatalyst with an abundance of oxygen vacancies achieved through the facile, one-step annealing of a Ru-exchanged ZIF-67 derivative. The compound exhibits ultra-high OER performance in acidic media, with a low overpotential of 169 mV at 10 mA cm^{-2} while maintaining excellent activity, even when exposed to a 50-h galvanostatic stability test at a constant current of 10 mA cm^{-2}. The dramatic enhancement in OER performance is mainly attributed to the abundance of oxygen vacancies and modulated electronic structure of the Co-doped RuO$_2$ that rely on a vacancy-related lattice oxygen oxidation mechanism (LOM) rather than adsorbate evolution reaction mechanism (AEM), as revealed and supported by experimental characterizations as well as density functional theory (DFT) calculations.

INTRODUCTION

Hydrogen is considered an ideal clean energy carrier to store electrical energy derived from renewable, intermittent power sources that has evoked significant interest and stimulated intensive investigations in the scientific literature. Furthermore, the conversion of hydrogen back into electrical energy can be efficiently performed in fuel cells to effectively harness the energy initially stored. Electrochemical water splitting, including hydrogen evolution reaction and oxygen evolution reaction (OER), provide an efficient and environmentally friendly way for large-scale hydrogen production with high purity. To date, alkaline water splitting technologies have been well established and are commercially available for industrial H$_2$ production (Jin et al., 2016; Suen et al., 2017; Zheng et al., 2016; Wang et al., 2018a, 2018b; Zhuang et al., 2019; Zhou et al., 2019). Nevertheless, compared with alkaline water splitting, acidic water splitting using proton exchange membrane (PEM) electrolyzer offers great advantages such as higher ionic conductivity, fewer unfavorable reactions, high voltage efficiency, and faster system response (Nong et al., 2015; Sardar et al., 2014). However, the scarcity of highly active and stable OER electrocatalysts in acidic condition greatly hinders the widespread commercialization of acidic water splitting. Ir oxide-based materials are considered as the state-of-the-art electrocatalysts for OER under acidic condition. For example, Ir-based double perovskites (Diaz-Morales et al., 2016), IrO$_x$/SrIrO$_3$ hybrid (Seitz et al., 2016), and pyrochlore-structured Ir-based oxide (Kim et al., 2017) were recently reported to be active and stable OER electrocatalysts in acidic condition. Unfortunately, their potential for commercialization is greatly hindered by the low production and high price of Ir. A possible alternative to Ir is the much cheaper Ru, which also shows high OER catalytic activity in acidic condition, such as the typical rutile-structured RuO$_2$ (Lee et al., 2012). However, many Ru-based electrocatalysts suffer from low stability in acidic condition owing to the over-oxidation of Ru into soluble RuO$_4$ moieties under the demanding oxidative environment (Kotz et al., 1983). Therefore, elaborate design or optimization of Ru-based systems with improved activity and stability is a matter of utmost urgency and a prospective area of research for the development of efficient and economically attractive acidic water splitting. To address this problem, in our previous work, we focused on altering RuO$_2$ surface atom arrangement and/or electronic structures that are pivotal to the catalytic performances. Accordingly, we fabricated hollow porous RuO$_2$ polyhedra (Su et al., 2018) and CrO$_2$-RuO$_2$ solid solution (Lin et al., 2019) materials that exhibit excellent OER performance. Specifically, CrO$_2$-RuO$_2$ solid solution possess a very low overpotential of 178 mV at 10 mA cm^{-2} and galvanostatic stability test of 10 h at the same current density in 0.5 M H$_2$SO$_4$. Recently, Lotsch and co-workers reported RuO$_2$ nanosheets with enhanced acidic OER activity and stability ascribing the increase in reactivity to the surface edges of RuO$_2$ (Laha et al., 2019).

Scheme 1. Illustration of the Synthesis of Co-doped RuO$_2$ Nanorods

Besides metal doping and morphological control, oxygen vacancies in transition metal oxides have been reported to enhance the electrocatalytic process. For example, Xu et al. created oxygen vacancies on Co$_3$O$_4$ nanosheets via a plasma-engraving strategy, revealing that the vacancies can significantly enhance the alkaline OER activity of the nanosheets (Xu et al., 2016, 2018). The authors proposed that the oxygen vacancies on the Co$_3$O$_4$ nanosheets surface could improve the electronic conductivity and create more active sites for OER. Very recently, Wang et al. (Huang et al., 2019) and Kolpak et al. (Yoo et al., 2018) proposed a vacancy-related lattice oxygen oxidation mechanism (LOM), which could bypass the limitation of the most commonly reported adsorbate evolution mechanism (AEM) having a minimum theoretical overpotential of 0.37 eV. In light of these studies, we attempted to synthesize RuO$_2$-based electrocatalyst that has abundant oxygen vacancies with optimized electronic structure for enhanced OER performance in acidic media. To achieve this target, we proposed to use some alien metal ions with different valence state to replace the Ru ions, which can simultaneously create oxygen vacancies and alter the electronic structures. Herein we chose Co because the lower oxidation states of Co dopants in the RuO$_2$ lattice require less O^{2-} ions to appropriately balance the charge, thus yielding oxygen vacancies. Metal-organic frameworks (MOFs) have been demonstrated to be versatile templates or precursors to prepare highly active electrocatalysts (Liu et al., 2017), such as N-doped porous carbon (Ma et al., 2016; Xia et al., 2016), metal oxides nanocomposites (Cai et al., 2017; Salunkhe et al., 2017), and carbon-coated nanosized metal alloys (Su et al., 2017). Based on this platform, we have successfully prepared a Co-doped RuO$_2$ nanorod electrocatalyst by annealing a Ru-exchange ZIF-67 amorphous composite. We selected ZIF-67 as a candidate because of its high surface area, accessible porosity that can facilitate ion exchange, and ease of synthesis (Banerjee et al., 2008; Gross et al., 2012; Qian et al., 2012). The synthetic route is briefly illustrated in Scheme 1. The resulting Co-doped RuO$_2$ nanorod exhibits an extremely low overpotential of 169 mV for OER in acidic environment at 10 mA cm^{-2} and excellent stability with a chronopotentiometry performance of over 50 h at the same current, outperforming the most active OER electrocatalysts reported to date. Based on the density functional calculations, we propose that the OER process on the compound undergoes a vacancy-related LOM, which enhances both the activity and stability.

RESULTS AND DISCUSSIONS

Synthesis and Characterization of Ru-ZIF-67 and Co-Doped RuO$_2$ Nanorods

ZIF-67 was synthesized via a facile procedure previously reported (Feng and Carreon, 2015) (see details in Methods section). The powder X-ray pattern (PXRD) and scanning electron microscope (SEM) image of the as-prepared product confirms that a pure ZIF-67 phase was obtained (Figures S1 and S2). The Co ions in ZIF-67 were exchanged by Ru ion (RuCl$_3$ was used as the Ru ion source) in THF solvent at room temperature
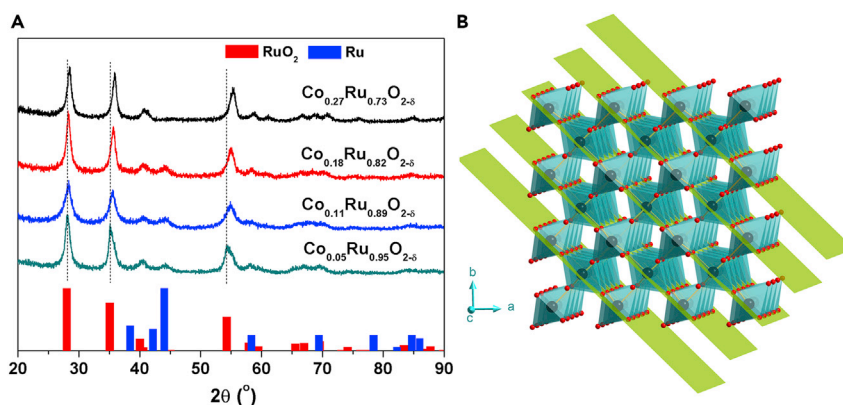
Figure 1. Structure Characterization of Co-doped RuO$_2$

(A) PXRD patterns of Co-doped RuO$_2$ samples with different Co content annealed at 350°C.

(B) Crystal structure of rutile RuO$_2$ viewed along the c axis. Yellow planes represent the (110) facets. Red ball, O; gray ball, Ru.

to obtain Ru-exchanged ZIF-67 (Ru-ZIF-67). The Ru content in the resulting product can be varied by controlling the amount of RuCl$_3$ reactant used for the exchange reaction. The resulting Ru-ZIF-67 is amorphous as revealed by the PXRD pattern and SEM image (Figures S3 and S4), which could be attributed to the significantly different coordination manner and environment of Ru and Co. In fact, crystal structure is not necessary for the following annealing treatment, which is associated with pyrolysis and atom rearrangements. Co-doped RuO$_2$ nanorods with different Co/Ru ratio can be obtained through further thermal decomposition of the as-prepared Ru-ZIF-67 powders in air at 350°C. Based on inductively coupled plasma-mass spectroscopy (ICP-MS) measurements, the formulas of the as-prepared RuO$_2$ samples are Co$_{0.27}$Ru$_{0.73}$O$_{2-\delta}$, Co$_{0.18}$Ru$_{0.82}$O$_{2-\delta}$, Co$_{0.11}$Ru$_{0.89}$O$_{2-\delta}$, and Co$_{0.04}$Ru$_{0.96}$O$_{2-\delta}$ (δ is used to balance the valence), respectively. Figure 1A shows the PXRD patterns of these samples, in which the major phase can be identified as rutile RuO$_2$ (JCPDS. No. 43-1027). Notably, the PXRD signals that belong to RuO$_2$ shift to the right when the Co content in the sample increases, suggesting that Co atoms have been successfully incorporated into the RuO$_2$ crystal lattice to form a rutile Co-doped RuO$_2$ phase with a concomitant lattice shrink. Figures 1B and S5 show the planes of RuO$_2$ corresponding to the labeled PXRD peaks. The *d* spaces of these planes decrease after the insertion of Co atoms that have a smaller size than that of the Ru atom. We further varied the annealing temperature for Co$_{0.11}$Ru$_{0.89}$O$_{2-\delta}$ to investigate the structural evolution of Co-doped RuO$_2$ nanocrystals. As shown in Figure S6, the content of metallic Ru can be decreased by increasing the annealing temperature and becomes negligible when the annealing temperature is increased to 500°C. The higher annealing temperatures lead to better crystallinity for the Co-doped RuO$_2$ as seen from the higher peak intensity and increased sharpness of the PXRD signals.

Transmission electron microscopy (TEM) was employed to characterize the morphology and structure of the Co-doped RuO$_2$ powders. As shown in Figures 2A–2D and S7–S9, all of the as-prepared Co-doped RuO$_2$ samples display nanorod-like shape morphology with a diameter of ~8 nm and length of ~20 nm. High-resolution TEM (HR-TEM) image (Figure 2E) clearly shows lattice fringes, indicating the high crystallinity of the Co-doped RuO$_2$ samples. Both the HR-TEM and the selected area electron diffraction (SAED) characterization (Figure 2F) confirm the rutile RuO$_2$ structure of Co-doped RuO$_2$ nanorods. High-angle annular dark-field scanning transmission microscopy (HAADF-STEM) was employed to analyze the elemental distribution over a single nanorod. As shown in Figure 2G, the elements of Ru, Co, and O were uniformly distributed over an entire single nanorod crystal, demonstrating the formation of rutile Co-doped RuO$_2$ phase (the mapping images for a wider region are shown in Figure S10), consistent with the finding from PXRD characterization. In addition, Co$_{0.11}$Ru$_{0.89}$O$_{2-\delta}$ (350) displays a typical type II isotherm with an H1 type hysteresis loop (Figure S11), which is characteristic for the aggregation of small particles. The calculated surface area for Co$_{0.11}$Ru$_{0.89}$O$_{2-\delta}$ (350) is 31.3 m^2 g^{-1}, larger than that of RuO$_2$ (8.9 m^2 g^{-1}).

OER Activity in Strong Acidic Media

The OER activity of Co-doped RuO$_2$ powders was investigated in a strong acidic media (0.5 M H$_2$SO$_4$) by use of a typical three-electrode electrochemical system containing a Pt wire as counter-electrode and an
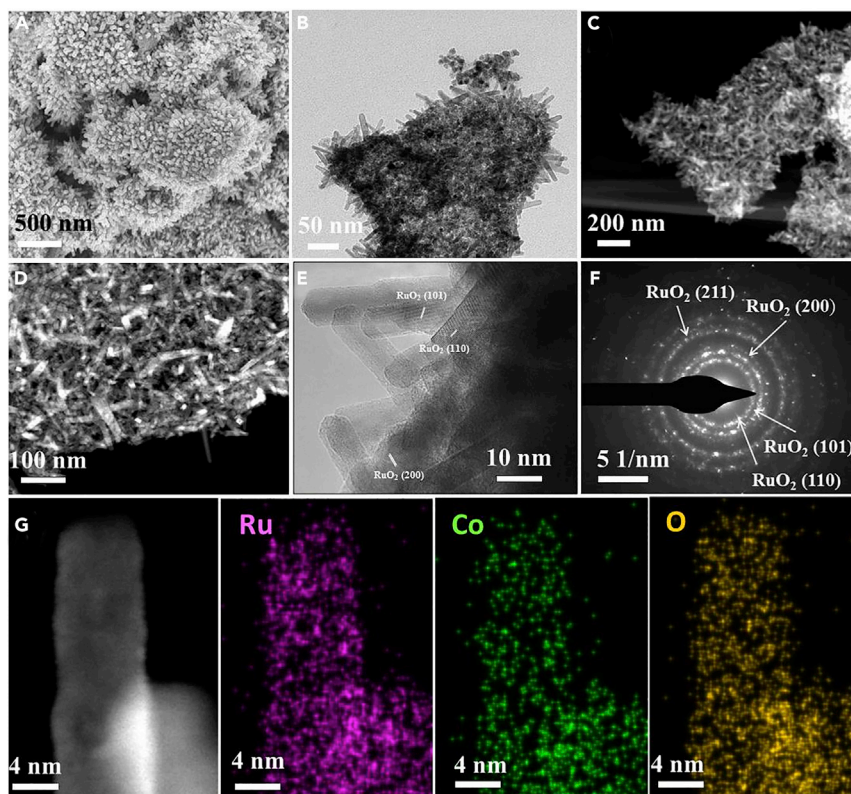
Figure 2. Morphology, Structure, and Element Mapping Images of $Co_{0.11}Ru_{0.89}O_2$ Annealed at 350°C
(A) SEM image.
(B) TEM image.
(C and D) Dark-field TEM images with small (C) and large (D) magnification levels.
(E) HR-TEM image.
(F) SAED image.
(G) HAADF-STEM image and the corresponding mapping images.

Hg/Hg$_2$SO$_4$ reference electrode (see details in Methods section). The Co-doped RuO$_2$-based electrodes were prepared by drop-casting a water/ethanol and Nafion-based ink of Co-doped RuO$_2$ on glassy carbon disk. We measured linear sweep voltammetry (LSV) curves at a scan rate of 5 mV s^{-1}. The Ohmic potential drop (iR) correction was performed to all experimental data to eliminate the effect of solution resistance, and the potentials were calibrated to the reversible hydrogen electrode (RHE) for comparison. Initially, we investigated the OER performance of Co-doped RuO$_2$ powders with different Co content to emphasize the effects of Co content on the OER catalysis of RuO$_2$ and to obtain a sample with optimum OER activity for further exploration. Figure 3A presents the LSV curves of $Co_{0.27}Ru_{0.73}O_{2-\delta}$, $Co_{0.18}Ru_{0.82}O_{2-\delta}$, $Co_{0.11}Ru_{0.89}O_{2-\delta}$, and $Co_{0.03}Ru_{0.97}O_{2-\delta}$ annealed at 350°C, where the rising current indicates the evolution of oxygen. As seen in Figure 3A, the OER activity is inversely proportional to Co content when the Co/Ru ratio is higher than 0.11:0.89, suggesting that the Ru atom is the catalytic center. Reasonably, a higher Co content will decrease the number of exposed catalytic Ru sites. However, when the Co/Ru ratio reduces to 0.04:0.96, the OER activity becomes relatively poor, thus emphasizing the significant role of Co dopant, which can induce oxygen vacancy and modify the electronic structure of Ru. Clearly, $Co_{0.11}Ru_{0.89}O_{2-\delta}$ (350) exhibited the best OER activity among the samples, with an overpotential of 169 mV at 10 mA cm^{-2}. We thus further altered the annealing temperature of $Co_{0.11}Ru_{0.89}O_{2-\delta}$ to realize the best annealing temperature for $Co_{0.11}Ru_{0.89}O_{2-\delta}$ to maximize the OER performance. As shown in Figure 3B, along with the rise of annealing temperature, the OER activity decreases successively. This decrease can be assigned to the lattice strain effects and/or reduced active crystal defects under higher annealing temperature and is supported by the increase in PXRD intensity and sharpness. Electrochemical impedance spectroscopy (EIS) measurements were also performed to assess the electrical resistance of $Co_{0.11}Ru_{0.89}O_{2-\delta}$ samples annealed at
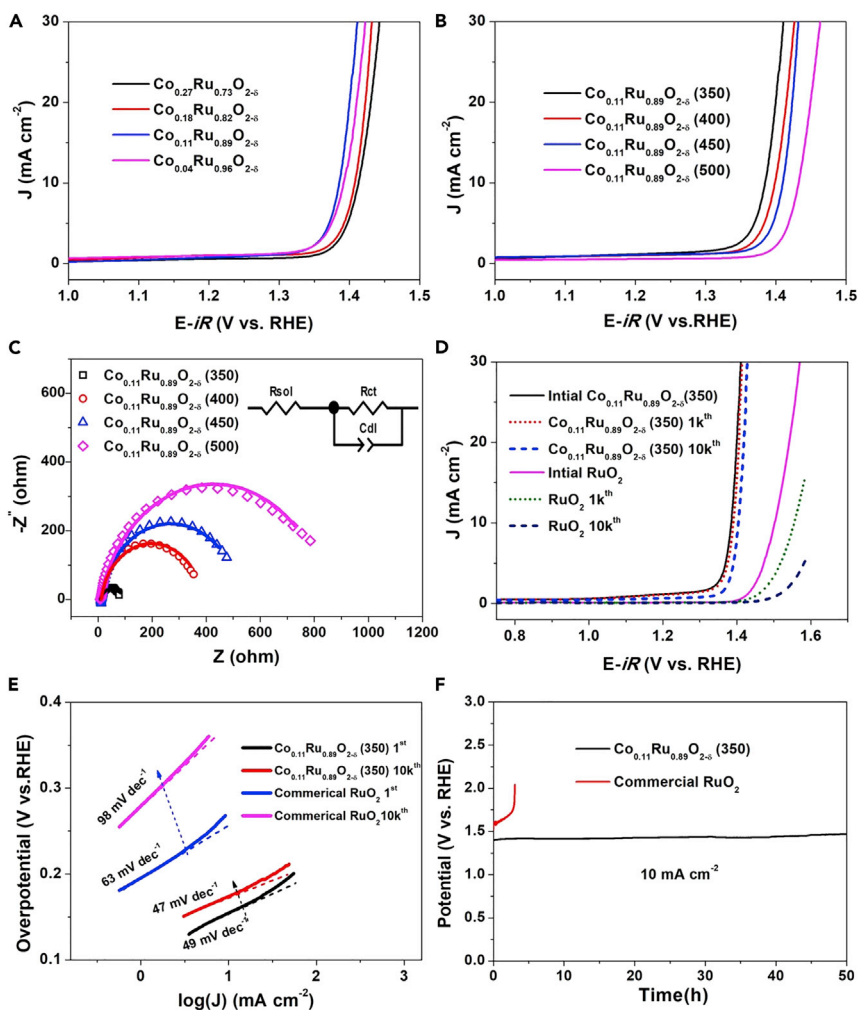
Figure 3. OER Performance of Co-doped RuO$_2$

(A) LSV curves of Co$_x$Ru$_{1-x}$O$_{2-\delta}$ annealed at 350°C.

(B) LSV curves of Co$_{0.11}$Ru$_{0.89}$O$_{2-\delta}$ annealed at different temperature.

(C) Impedances of Co$_{0.11}$Ru$_{0.89}$O$_{2-\delta}$ annealed at different temperature.

(D) LSV curves of Co$_{0.11}$Ru$_{0.89}$O$_{2-\delta}$ (350) and commercial RuO$_2$ before and after CV cycling measurements.

(E) Tafel plots of Co$_{0.11}$Ru$_{0.89}$O$_{2-\delta}$ (350) and commercial RuO$_2$ before and after CV cycling measurements.

(F) Chronopotentiometry test of Co$_{0.11}$Ru$_{0.89}$O$_{2-\delta}$ (350) and commercial RuO$_2$.

different temperature. As shown in Figure 3C, all the Nyquist plots display a depressed semicircle, suggesting a charge-transfer process during the OER. These Nyquist plots were further fitted to analyze the electrical resistance by a simple equivalent electrical circuit as shown in the inset in Figure 3C (Audichon et al., 2016; Harrington and van den Driessche, 2011). Co$_{0.11}$Ru$_{0.89}$O$_{2-\delta}$ (350) exhibits the smallest semicircle radius compared with other catalysts, implying the smallest electric resistance and fastest charge transfer rate OER kinetics at the interface.

As demonstrated by the above results and discussion, Co$_{0.11}$Ru$_{0.89}$O$_{2-\delta}$ (350) is the optimized material as it possesses the highest OER performance among those samples with varying Co content or annealing temperatures. We further tested the stability of Co$_{0.11}$Ru$_{0.89}$O$_{2-\delta}$ (350) by cycling the catalyst between 1.2 and 1.6 V at a sweep rate of 100 mV s^{-1} in 0.5 M H$_2$SO$_4$ for 10,000 cycles. As shown in Figure 3D, after 10,000 cycles, the overpotential of Co$_{0.11}$Ru$_{0.89}$O$_{2-\delta}$ (350) was 184 mV, only a 15-mV increase relative to the initial overpotential. For further comparison, the OER performance of commercial RuO$_2$ with a particle size of ~30 nm was also tested at identical conditions. RuO$_2$ displays much lower OER activity, with an overpotential up to 273 mV to drive the current density of 10 mA cm^{-2}. Moreover, after 10,000 cycles, the OER activity

of RuO_2 is dramatically reduced and becomes negligible compared with the initial OER activity, revealing poor stability for OER in acidic media. These results for commercial RuO_2 are consistent with those seen in the literature (Kim et al., 2017; Audichon et al., 2016; Li et al., 2017). In addition, considering that the OER activity is correlated to the number of exposed sites, we further plotted the LSV of $Co_{0.11}Ru_{0.89}O_{2-\delta}$ (350) and RuO_2 with respect to the calculated surface areas (Figure S12). The results show that the enhanced OER performance of $Co_{0.11}Ru_{0.89}O_{2-\delta}$ (350) is not merely increased by the surface area. In contrast, the enhanced intrinsic activity arises from oxygen vacancies and the Co dopant plays a much more important role.

Figure 3E shows the Tafel plots of $Co_{0.11}Ru_{0.89}O_{2-\delta}$ (350) and RuO_2 before and after 10,000 cycles. The Tafel slope for RuO_2 of the initial cycle is 63 mV dec^{-1} and dramatically rises to 98 mV dec^{-1} after 10,000 cycles. For $Co_{0.11}Ru_{0.89}O_{2-\delta}$ (350), the Tafel slope slightly decreases from 49 to 47 mV dec^{-1} after 10,000 cycles, implying that the OER kinetics of $Co_{0.11}Ru_{0.89}O_{2-\delta}$ (350) after 10,000 cycles is slightly faster than that of initial $Co_{0.11}Ru_{0.89}O_{2-\delta}$ (350). The smaller and unchanged Tafel slope of $Co_{0.11}Ru_{0.89}O_{2-\delta}$ (350) suggests a faster and much more stable OER kinetic rate than RuO_2. Ultimately, to further confirm the big difference in stability of $Co_{0.11}Ru_{0.89}O_{2-\delta}$ (350) and RuO_2, chronopotentiometry was examined under a constant current density of 10 mA cm^{-2}. Figure 3F presents the corresponding potential change for both $Co_{0.11}Ru_{0.89}O_{2-\delta}$ (350) and RuO_2. Clearly, RuO_2 loses OER activity in less than 3 h; on the contrary, $Co_{0.11}Ru_{0.89}O_{2-\delta}$ (350) remains essentially stable throughout the 50-h galvanostatic stability test. We also measured the chronopotentiometric curve under a higher current density of 50 mA cm^{-2}. As shown in Figure S13, $Co_{0.11}Ru_{0.89}O_{2-\delta}$ (350) remains essentially stable throughout the 8-h galvanostatic stability test. Furthermore, as shown in Figure S14, the Co/Ru ratio before cyclic voltammetry (CV) is 0.124/0.876, generally consistent with the ICP result (Co/Ru = 0.11/0.89). After CV cycles, the Co/Ru ratio shows a very slight decrease, with a value of 0.107/0.893 (Figure S15), indicating the high stability of $Co_{0.11}Ru_{0.89}O_2$ (350). In addition, the morphology of $Co_{0.11}Ru_{0.89}O_2$ (350) after 10,000 CV cycles remains unchanged (Figure S16). These results demonstrate that $Co_{0.11}Ru_{0.89}O_{2-\delta}$ (350) is stable in 0.5 M H_2SO_4 at the oxidizing potential during the OER process. For comparison, we summarized the reported materials with high OER activity in acidic media in Table S1. Notably, $Co_{0.11}Ru_{0.89}O_{2-\delta}$ (350) presents a record low overpotential and outperforms IrO_2-based catalysts, which represent the state-of-the-art electrocatalyst for OER in acidic media.

Origin of OER Activity and Stability

We first carried out X-ray photoelectron spectroscopy (XPS) analysis to assess the surface chemical state of $Co_{0.11}Ru_{0.89}O_{2-\delta}$ (350). For comparison, XPS of commercial RuO_2 was also measured. As shown in Figure 4A, the XPS peaks for Ru 3d of $Co_{0.11}Ru_{0.89}O_{2-\delta}$ (350) and RuO_2 can be deconvoluted into two sets of doublet peaks for Ru $3d_{5/2}$, $3d_{3/2}$, their satellite peaks, and two single peaks for C1s (arising from corrosion carbon) (Morgan, 2015). For RuO_2, the primary Ru $3d_{5/2}$ and $3d_{3/2}$ peaks of RuO_2 center at 280.6 and 284.8 eV, respectively, consistent with those reported in the literature (Sarma and Rao, 1980; Shen et al., 1991). As for Ru 3d of $Co_{0.11}Ru_{0.89}O_{2-\delta}$ (350), a small shift to higher binding energy can be clearly observed, which may be attributed to a higher electron density at the Ru sites. As mentioned earlier, there is a small portion of metallic Ru in our sample as determined by PXRD characterizations. However, the corresponding XPS peaks for metallic Ru are nearly invisible possibly because the majority of species in the outer surface are aggregated $Co_{0.11}Ru_{0.89}O_{2-\delta}$ (350) particles in the RuO_2 phase. In the annealing process, the outer surface of the sample is directly exposed to air largely increasing the probability of generating metal oxides. The Co 2p spectrum of $Co_{0.11}Ru_{0.89}O_{2-\delta}$ (350) is shown in Figure S17. For comparison, we also prepared a sample by annealing pure ZIF-67 using the same procedure for preparing $Co_{0.11}Ru_{0.89}O_{2-\delta}$ (350). The structure of the resulting powder is identified as Co_3O_4 (Figure S18). As shown in Figure S14, the main peak of Co 2p is shifted toward higher binding energy state compared with that of Co_3O_4 derived from ZIF-67, suggesting a relatively higher oxidation state of Co doped into $Co_{0.11}Ru_{0.89}O_{2-\delta}$ (350) attributed to the electron withdrawing effect of Ru^{4+} in the lattice. O 1s spectra for $Co_{0.11}Ru_{0.89}O_{2-\delta}$ (350) and RuO_2 are shown in Figure 4B. For RuO_2, the O 1s XPS peak can be deconvoluted into four peaks, corresponding to different type of O species. The main peak centered at 529.2 eV corresponds to the Ru-O in the lattice, and the shoulder peak centered at 530.5 eV can be assigned to the OH^- ions that integrated into the outer surface of RuO_2. The higher binding energy peak centered at 531.9 eV is attributed to the surface oxygen vacancies species, which is often observed on metal oxides (Dupin et al., 2000; Uhlenbrock et al., 1992). The small peak centered at 533.3 eV originates from the adsorbed H_2O molecules (Dupin et al., 2000). For $Co_{0.11}Ru_{0.89}O_{2-\delta}$ (350), the O 1s peak can be deconvoluted into three peaks, corresponding to the Ru-O, OH^-, and oxygen vacancy species, respectively.
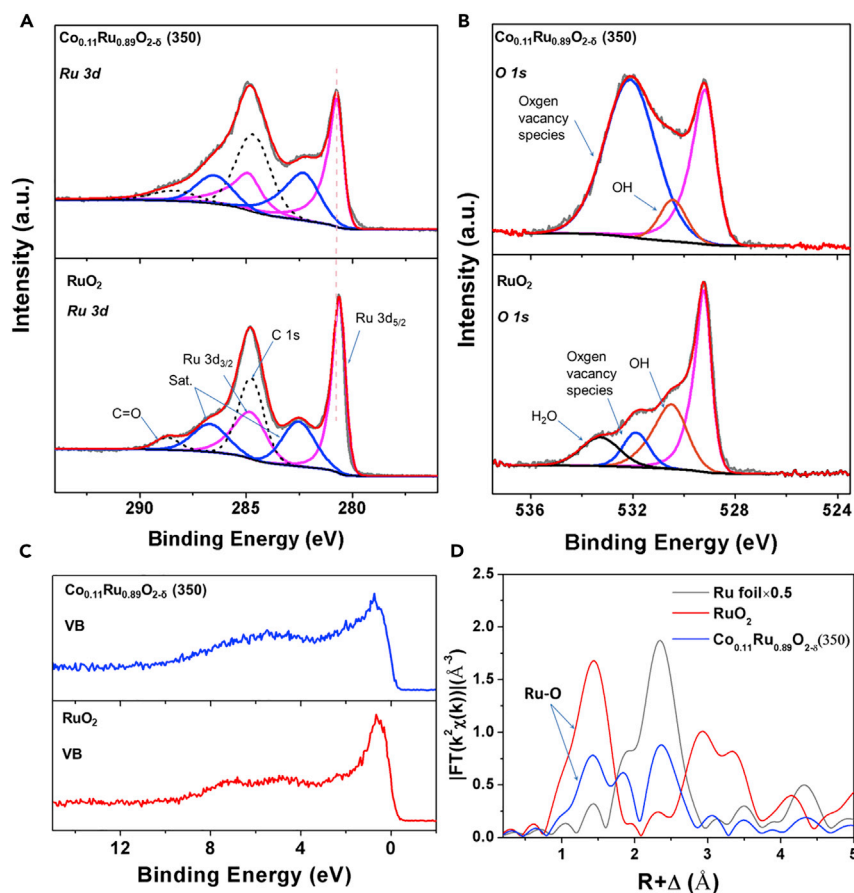
Figure 4. Chemical State and Structure Analysis of $Co_{0.11}Ru_{0.89}O_{2-\delta}$ (350)

(A) Ru 3d XPS profiles of $Co_{0.11}Ru_{0.89}O_{2-\delta}$ (350) and RuO_2.

(B) O 1s XPS profiles of $Co_{0.11}Ru_{0.89}O_{2-\delta}$ (350) and RuO_2.

(C) Valence band XPS profiles of $Co_{0.11}Ru_{0.89}O_{2-\delta}$ (350) and RuO_2.

(D) Fourier transformed EXAFS spectra of Ru K-edge for $Co_{0.11}Ru_{0.89}O_{2-\delta}$ (350), RuO_2, and Ru foil.

We can find that the peak for oxygen vacancy species is much stronger than that of RuO_2, suggesting that a larger number of oxygen vacancies exist on the $Co_{0.11}Ru_{0.89}O_{2-\delta}$ (350) surface. The increase of oxygen vacancies on $Co_{0.11}Ru_{0.89}O_{2-\delta}$ (350) arises from the lower oxidation state of Co dopants in the RuO_2 lattice that require less O^{2-} ions to appropriately balance the charge. In many cases, oxygen vacancies species can significantly enhance the OER activity by dramatically improving the electronic conductivity that leads to the creation of more active sites (Xu et al., 2016). In addition, compared with RuO_2, $Co_{0.11}Ru_{0.89}O_{2-\delta}$ (350) shows a broadened valence band (VB) spectra (Figure 4C), suggesting that the incorporation of Co dopants not only introduces the oxygen vacancies but also modulates the electronic structure of RuO_2. The XPS wide-scan spectrum of $Co_{0.11}Ru_{0.89}O_{2-\delta}$ (350) is shown in Figure S19. In addition, we also measured the XPS spectra for Co and Ru elements of $Co_{0.11}Ru_{0.89}O_{2-\delta}$ (350) after stability test. As shown in Figures S20 and S21, the XPS spectra of Co and Ru after stability test remained generally unchanged in both position and shape, indicating the high stability of $Co_{0.11}Ru_{0.89}O_{2-\delta}$ (350).

To investigate the local structure of $Co_{0.11}Ru_{0.89}O_{2-\delta}$ (350), X-ray absorption spectroscopy (XAS) characterization was further employed (Figure S22). The Fourier transformed (FT) radial structure based on the k^2-weighted extended X-ray absorption fine structure (EXAFS) is displayed in Figure 4D. The peak at ~1.5 Å corresponds to Ru-O bonds. Interestingly, compared with RuO_2, the intensity of this peak for $Co_{0.11}Ru_{0.89}O_{2-\delta}$ (350) distinctly decreased, which is ascribed to the coordination deficiency from Ru, revealing the existence of abundant oxygen vacancies in $Co_{0.11}Ru_{0.89}O_{2-\delta}$ (350). Note that the Ru-Ru peak is also present, which is consistent with the PXRD results.
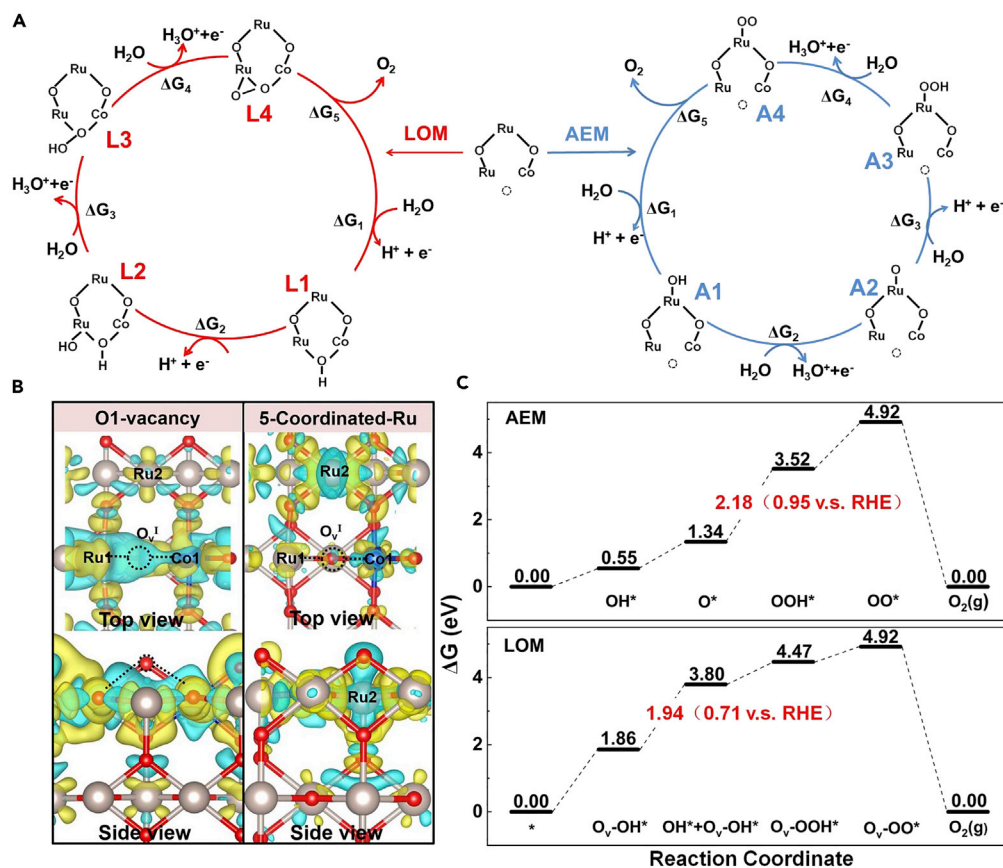
Figure 5. Comparison of OER Mechanisms with the Different Local Configurations

(A) Proposed LOM and AEM mechanisms. L1 is thermally favorable energetically than A2.

(B) The charge energy difference of A1 and L1 to illustrate the lower electron depletion on O_v^I than Ru2, which is attributed to the higher activity of O_v^I in OER process.

(C) The free energy diagrams of the two mechanisms of LOM and AEM. The rate-determining barriers together with that versus RHE are denoted.

Finally, we carried out density functional theory (DFT) calculations to gain more insights into the excellent OER activity of Co-RuO$_2$. Based on previous studies that RuO$_2$ (110) was identified as the most stable surface with the lowest surface energy among various facets (Su et al., 2018; Fang and Liu, 2010; Wei and Liu, 2011), we constructed a (110) surface model of Co$_x$Ru$_{1-x}$O$_{2-x}$ (x = 0.1) to simulate the experimentally obtained material. O vacancy is created to maintain the total charge balance induced by different valence states of Co and Ru atoms. As shown in Figure S23, two possible types of O vacancies were located on different sites: O_v^I formed by the substitution of 6-coordinated Ru and O_v^{II} formed by the substitution of 5-coordinated Ru. The comparison of the formation energies indicates that O_v^I vacancy sites are dominant and mainly participate in the subsequent OER process owing to its 0.50 eV lower formation energy than that of O_v^{II} sites.

To address the role of oxygen vacancies in OER, the activity of the neighbored 5-coordinated Ru is definitely inevitable to be compared. Therefore, two possible competing OER processes via O_v^I in LOM and 5-coordinated Ru in AEM were comparatively investigated to explore the preferred lower free energy path. As demonstrated in Figure 5A, five elementary steps are taken into account involving four electrochemical electron transfer steps ($\Delta G_1 \sim \Delta G_4$) and one non-electrochemical O$_2$ desorption step (ΔG_5) in both processes. For the initial adsorption of upcoming H$_2$O molecule, the intermediate L1 (O_v^I-OH) in LOM and intermediate A1 (Ru-OH) in AEM were formed on O_v^I and 5-coordinated Ru sites, respectively. The lower adsorption energy (0.71 eV) of L1 than A1 reveals that H$_2$O preferred to react with O_v^I vacancy rather than the Ru site. It is well reasonable because O_v^I vacancy between the two unsaturated cations (Ru1 and Co1 in Figure S24) on

the surface possesses lower electron depletion (blue contour) in Figure 5B to bind with H_2O molecules, thus yielding lower adsorption energy of L1 to proceed the following OER steps in LOM mechanism.

Another important factor to evaluate the effect of O vacancy on OER process is free energy variation of the rate-determining step (RDS) in both LOM and AEM, as plotted in Figure 5C. Along the LOM reaction path, the formation of Ru(OH)-O_v^I(OH) after the second H_2O attacking was identified as RDS, which yielded a free energy barrier of 0.71 eV versus RHE. The RDS in AEM occurred on the formation of *OOH on the 5-coordinated Ru with yielding a free energy barrier of 0.95 eV versus RHE. Clearly, the corresponding 0.24 eV lower energy barrier of RDS in LOM suggested that the OER would preferentially undertake O vacancy site rather than the 5-coordinated Ru site. Moreover, we believe that the enhanced stability is also associated with the LOM pathway. The participation of O vacancy can effectively avoid the over-oxidation of Ru to the soluble RuO_4, which is deemed as the major reason for the instability of RuO_2 electrocatalyst governed by AEM in the acidic conditions.

The density of states of RuO_2 and Co-doped RuO_2 were compared and provided in Figure S25 to further understand the inherent electron variation on O vacancies. The binding region between −2.0 eV and the Fermi level was obviously broadened in the Co-doped RuO_2, which was well consistent with the observed XPS VB results. Actually, both IrO_2 and Cu-doped RuO_2 electrocatalysts were previously found to promote OER activity by broadening the binding regions (Su et al., 2018; Sun et al., 2015). It is well accepted that the *p*-band center of O is an effective descriptor to evaluate OER performance (Grimaud et al., 2013). Our calculated *p*-band centers were −4.57 eV in RuO_2 and −3.03 eV in $Ru_{1-x}Co_xO_{2-x}$, showing a higher energy shift toward the Fermi level upon the creation of O vacancy by Co dopant. According to *p*-band center theory, $Ru_{1-x}Co_xO_{2-x}$ with *p*-band center closer to the Fermi level exhibits higher OER catalytic activity.

Conclusion

In summary, by use of Co-based MOF, we have developed a nanorod-like Co-doped RuO_2 electrocatalyst with superior OER performance in acidic condition. Impressively, this compound outperforms the state-of-the-art IrO_2-based electrocatalyst and the currently reported RuO_2-based electrocatalysts by demonstrating an ultralow overpotential (169 mV) and excellent stability. The abundance of oxygen vacancies together with the modulated electronic structure contribute to the superior OER activity, as revealed by both experimental characterizations and DFT calculations. We show that the OER preferentially proceeds via the LOM pathway by passing a lower RDS barrier (0.24 eV) in the assistance of O vacancies than reacting on 5-coordinated Ru. This OER enhancement is attributed to larger charge depletion on O vacancies and higher energy shift toward the Fermi level of *p*-band center. Our study puts forward the potential of using doped RuO_2-based materials to confront the challenges in acidic OER process.

Limitations of the Study

Based on the combination of XPS, XAS, and DFT, oxygen vacancy has been interpreted as a key contributor to the excellent acidic OER activity and stability. However, to get an in-depth sight of the effect of oxygen vacancy, an *in situ* characterization of the oxygen vacancy is still needed but is very challenging.

METHODS

All methods can be found in the accompanying Transparent Methods supplemental file.

SUPPLEMENTAL INFORMATION

Supplemental Information can be found online at https://doi.org/10.1016/j.isci.2019.100756.

ACKNOWLEDGMENTS

AUTHOR CONTRIBUTIONS

L.C. and Y.L. designed the project and wrote the manuscript; Y.T. and Y.L. carried out the experiments; S.W. and Q.Z. carried out DFT calculations; Q.Z. wrote the computational part of the manuscript; L.Z. performed

the XAS experiments and data analysis. E.V., L.C., and X.L. provided helpful suggestions and polished the manuscript. All authors discussed the results and commented on the manuscript.

REFERENCES

Audichon, T., Napporn, T.W., Canaff, C., Morais, C., Comminges, C., and Kokoh, K.B. (2016). IrO2 Coated on RuO2 as efficient and stable electroactive nanocatalysts for electrochemical water splitting. J. Phys. Chem. C 120, 2562–2573.

Banerjee, R., Phan, A., Wang, B., Knobler, C., Furukawa, H., O'Keeffe, M., and Yaghi, O.M. (2008). High-throughput synthesis of zeolitic imidazolate frameworks and application to CO2 capture. Science 319, 939–943.

Cai, D.P., Zhan, H.B., and Wang, T.H. (2017). MOF-derived porous ZnO/ZnFe2O4 hybrid nanostructures as advanced anode materials for lithium ion batteries. Mater. Lett. 197, 241–244.

Diaz-Morales, O., Raaijman, S., Kortlever, R., Kooyman, P.J., Wezendonk, T., Gascon, J., Fu, W.T., and Koper, M.T. (2016). Iridium-based double perovskites for efficient water oxidation in acid media. Nat. Commun. 7, 12363.

Dupin, J.C., Gonbeau, D., Vinatier, P., and Levasseur, A. (2000). Systematic XPS studies of metal oxides, hydroxides and peroxides. Phys. Chem. Chem. Phys. 2, 1319–1324.

Fang, Y.H., and Liu, Z.P. (2010). Mechanism and Tafel lines of electro-oxidation of water to oxygen on RuO2(110). J. Am. Chem. Soc. 132, 18214–18222.

Feng, X.H., and Carreon, M.A. (2015). Kinetics of transformation on ZIF-67 crystals. J. Cryst. Growth 418, 158–162.

Grimaud, A., May, K.J., Carlton, C.E., Lee, Y.L., Risch, M., Hong, W.T., Zhou, J.G., and Shao-Horn, Y. (2013). Double perovskites as a family of highly active catalysts for oxygen evolution in alkaline solution. Nat. Commun. 4, 2439.

Gross, A.F., Sherman, E., and Vajo, J.J. (2012). Aqueous room temperature synthesis of cobalt and zinc sodalite zeolitic imidizolate frameworks. Dalton Trans. 41, 5458–5460.

Harrington, D.A., and van den Driessche, P. (2011). Mechanism and equivalent circuits in electrochemical impedance spectroscopy. Electrochim. Acta 56, 8005–8013.

Huang, Z.F., Song, J.J., Du, Y.H., Xi, S.B., Dou, S., Nsanzimana, J.M.V., Wang, C., Xu, Z.C.J., and Wang, X. (2019). Chemical and structural origin of lattice oxygen oxidation in Co-Zn oxyhydroxide oxygen evolution electrocatalysts. Nat. Energy 4, 329–338.

Jin, Y.S., Wang, H.T., Li, J.J., Yue, X., Han, Y.J., Shen, P.K., and Cui, Y. (2016). Porous MoO2 nanosheets as non-noble bifunctional electrocatalysts for overall water splitting. Adv. Mater. 28, 3785–3790.

Kim, J., Shih, P.C., Tsao, K.C., Pan, Y.T., Yin, X., Sun, C.J., and Yang, H. (2017). High-Performance Pyrochlore-type yttrium ruthenate electrocatalyst for oxygen evolution reaction in acidic media. J. Am. Chem. Soc. 139, 12076–12083.

Kotz, R., Lewerenz, H.J., and Stucki, S. (1983). XPS studies of oxygen evolution on Ru and RuO2 anodes. J. Electrochem. Soc. 130, 825–829.

Laha, S., Lee, Y., Podjaski, F., Weber, D., Duppel, V., Schoop, L.M., Pielnhofer, F., Scheurer, C., Muller, K., Starke, U., et al. (2019). Ruthenium oxide nanosheets for enhanced oxygen evolution catalysis in acidic medium. Adv. Energy Mater. 9, 1803795.

Lee, Y., Suntivich, J., May, K.J., Perry, E.E., and Shao-Horn, Y. (2012). Synthesis and activities of rutile IrO2 and RuO2 nanoparticles for oxygen evolution in acid and alkaline solutions. J. Phys. Chem. Lett. 3, 399–404.

Li, G.Q., Li, S.T., Ge, J.J., Liu, C.P., and Xing, W. (2017). Discontinuously covered IrO2-RuO2@Ru electrocatalysts for the oxygen evolution reaction: how high activity and long-term durability can be simultaneously realized in the synergistic and hybrid nano-structure. J. Mater. Chem. A 5, 17221–17229.

Lin, Y.C., Tian, Z.Q., Zhang, L.J., Ma, J.Y., Jiang, Z., Deibert, B.J., Ge, R.X., and Chen, L. (2019). Chromium-ruthenium oxide solid solution electrocatalyst for highly efficient oxygen evolution reaction in acidic media. Nat. Commun. 10, 162.

Liu, J., Zhu, D., Guo, C., Vasileff, A., and Qiao, S.-Z. (2017). Design strategies toward advanced MOF-Derived electrocatalysts for energy-conversion reactions. Adv. Energy Mater. 7, 1700518.

Ma, X., Zhou, Y.X., Liu, H., Li, Y., and Jiang, H.L. (2016). A MOF-derived Co-CoO@N-doped porous carbon for efficient tandem catalysis: dehydrogenation of ammonia borane and hydrogenation of nitro compounds. Chem. Commun. 52, 7719–7722.

Morgan, D.J. (2015). Resolving ruthenium: XPS studies of common ruthenium materials. Surf. Interface Anal. 47, 1072–1079.

Nong, H.N., Oh, H.S., Reier, T., Willinger, E., Willinger, M.G., Petkov, V., Teschner, D., and Strasser, P. (2015). Oxide-supported IrNiO(x) core-shell particles as efficient, cost-effective, and stable catalysts for electrochemical water splitting. Angew. Chem. Int. Ed. 54, 2975–2979.

Qian, J.F., Sun, F.A., and Qin, L.Z. (2012). Hydrothermal synthesis of zeolitic imidazolate framework-67 (ZIF-67) nanocrystals. Mater. Lett. 82, 220–223.

Salunkhe, R.R., Kaneti, Y.V., and Yamauchi, Y. (2017). Metal-Organic Framework-Derived Nanoporous metal oxides toward supercapacitor applications: progress and prospects. ACS Nano 11, 5293–5308.

Sardar, K., Petrucco, E., Hiley, C.I., Sharman, J.D., Wells, P.P., Russell, A.E., Kashtiban, R.J., Sloan, J., and Walton, R.I. (2014). Water-splitting electrocatalysis in acid conditions using ruthenate-iridate pyrochlores. Angew. Chem. Int. Ed. 53, 10960.

Sarma, D.D., and Rao, C.N.R. (1980). Xpes studies of oxides of 2nd-row and 3rd-row transition-metals including rare-earths. J. Electron Spectrosc. 20, 25–45.

Seitz, L.C., Dickens, C.F., Nishio, K., Hikita, Y., Montoya, J., Doyle, A., Kirk, C., Vojvodic, A., Hwang, H.Y., Norskov, J.K., and Jaramillo, T.F. (2016). A highly active and stable IrOx/SrIrO3 catalyst for the oxygen evolution reaction. Science 353, 1011.

Shen, J.Y., Adnot, A., and Kaliaguine, S. (1991). An ESCA study of the interaction of oxygen with the surface of ruthenium. Appl. Surf. Sci. 51, 47–60.

Su, J.W., Yang, Y., Xia, G.L., Chen, J.T., Jiang, P., and Chen, Q.W. (2017). Ruthenium-cobalt nanoalloys encapsulated in nitrogen-doped graphene as active electrocatalysts for producing hydrogen in alkaline media. Nat. Commun. 8, 14969.

Su, J.W., Ge, R.X., Jiang, K.M., Dong, Y., Hao, F., Tian, Z.Q., Chen, G.X., and Chen, L. (2018). Assembling ultrasmall copper-doped ruthenium oxide nanocrystals into hollow porous polyhedra: highly robust electrocatalysts for oxygen evolution in acidic Media. Adv. Mater. 30, 1801351.

Suen, N.T., Hung, S.F., Quan, Q., Zhang, N., Xu, Y.J., and Chen, H.M. (2017). Electrocatalysis for the oxygen evolution reaction: recent

development and future perspectives. Chem. Soc. Rev. *46*, 337–365.

Sun, W., Song, Y., Gong, X.Q., Cao, L.M., and Yang, J. (2015). An efficiently tuned d-orbital occupation of IrO2 by doping with Cu for enhancing the oxygen evolution reaction activity. Chem. Sci. *6*, 4993–4999.

Uhlenbrock, S., Scharfschwerdt, C., Neumann, M., Illing, G., and Freund, H.J. (1992). The influence of defects on the Ni-2p and O-1s XPS of Nio. J. Phys. Condens. Mater. *4*, 7973–7978.

Wang, X., Zhuang, L.Z., Jia, Y., Liu, H.L., Yan, X.C., Zhang, L.Z., Yang, D.J., Zhu, Z.H., and Yao, X.D. (2018a). Plasma-triggered synergy of exfoliation, phase transformation, and surface engineering in cobalt diselenide for enhanced water oxidation. Angew. Chem. Int. Ed. *130*, 16659–16663.

Wang, X., Zhuang, L.Z., He, T.W., Jia, Y., Zhang, L.Z., Yan, X.C., Gao, M.R., Du, A.J., Zhu, Z.H., Yao, X.D., and Yu, S.-H. (2018b). Grafting cobalt diselenide on defective graphene for enhanced oxygen evolution reaction. iScience *7*, 145–153.

Wei, G.F., and Liu, Z.P. (2011). Towards active and stable oxygen reduction cathodes: a density functional theory survey on Pt2M skin alloys. Energy Environ. Sci. *4*, 1268–1272.

Xia, B.Y., Yan, Y., Li, N., Wu, H.B., Lou, X.W., and Wang, X. (2016). A metal-organic framework-derived bifunctional oxygen electrocatalyst. Nat. Energy *1*, 15006.

Xu, L., Jiang, Q.Q., Xiao, Z.H., Li, X.Y., Huo, J., Wang, S.Y., and Dai, L.M. (2016). Plasma-engraved Co3O4 nanosheets with oxygen vacancies and high surface area for the oxygen evolution reaction. Angew. Chem. Int. Ed. *55*, 5277–5281.

Xu, L., Zou, Y.Q., Xiao, Z.H., and Wang, S.Y. (2018). Transforming Co3O4 nanosheets into porous N-doped CoxOy nanosheets with oxygen vacancies for the oxygen evolution reaction. J. Energy Chem. *35*, 24–29.

Yoo, J.S., Rong, X., Liu, Y.S., and Kolpak, A.M. (2018). Role of lattice oxygen participation in understanding trends in the oxygen evolution reaction on perovskites. ACS Catal. *8*, 4628–4636.

Zheng, Y., Jiao, Y., Zhu, Y.H., Li, L.H., Han, Y., Chen, Y., Jaroniec, M., and Qiao, S.Z. (2016). High electrocatalytic hydrogen evolution activity of an anomalous ruthenium catalyst. J. Am. Chem. Soc. *138*, 16174–16181.

Zhou, P., He, J.Y., Zou, Y.Q., Wang, Y.Y., Xie, C., Chen, R., Zang, S.Q., and Wang, S.Y. (2019). Single-crystalline layered double hydroxides with rich defects and hierarchical structure by mild reduction for enhancing the oxygen evolution reaction. Sci. China Chem. *62*, https://doi.org/10.1007/s11426-019-9511-x.

Zhuang, L.Z., Jia, Y., Liu, H.L., Wang, X., Hocking, R.K., Liu, H.W., Chen, J., Ge, L., Zhang, L.Z., Li, M.R., et al. (2019). Defect-induced Pt–Co–Se coordinated sites with highly asymmetrical electronic distribution for boosting oxygen-involving electrocatalysis. Adv. Mater. *31*, 1805581.

Supplemental Information

A Co-Doped Nanorod-like RuO$_2$

Electrocatalyst with Abundant Oxygen

Vacancies for Acidic Water Oxidation

Yuanyuan Tian, Shuo Wang, Ever Velasco, Yueping Yang, Lujie Cao, Linjuan Zhang, Xing Li, Yichao Lin, Qiuju Zhang, and Liang Chen
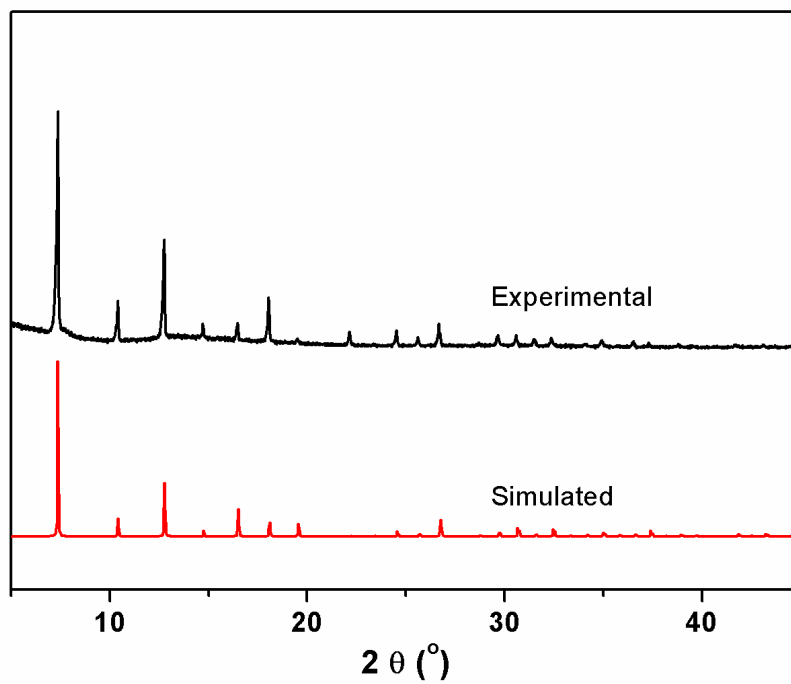
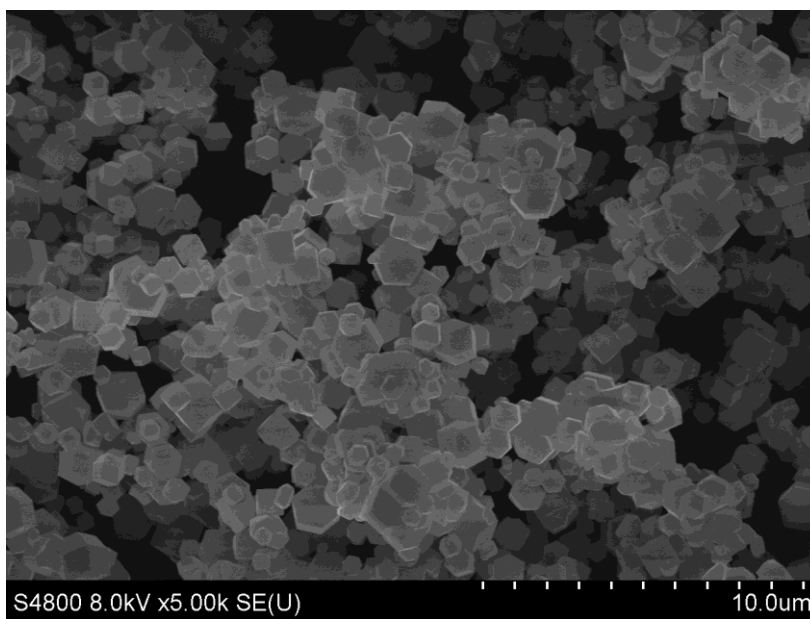Figure S1. PXRD pattern of as-prepared ZIF-67. Related to Scheme 1.

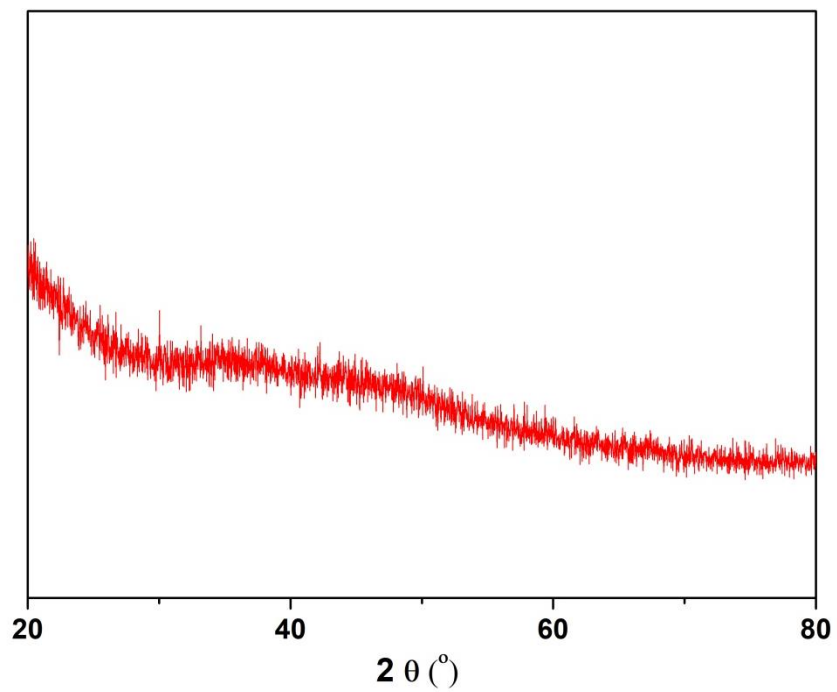Figure S2. SEM image of as-prepared ZIF-67. Related to Scheme 1.

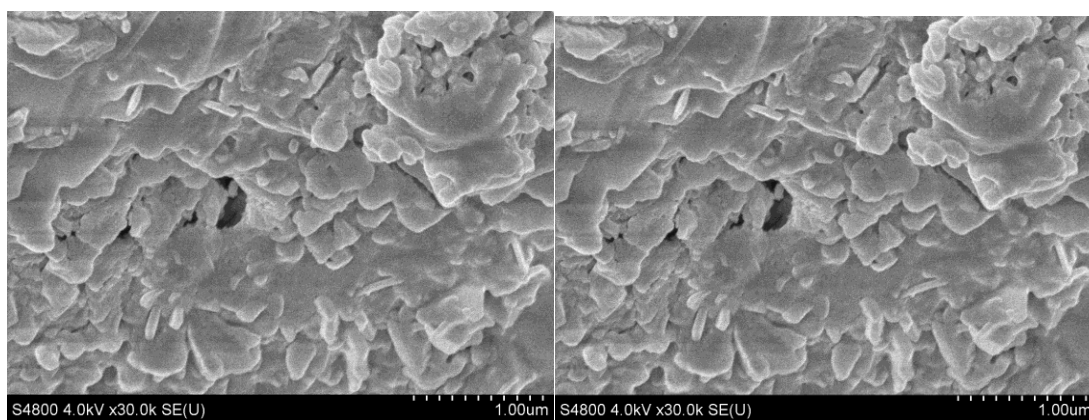Figure S3. PXRD pattern of Ru-ZIF-67-C. Related to Figure 1.

Figure S4. SEM images of Ru-ZIF-67-B and C. Related to Figure 1.
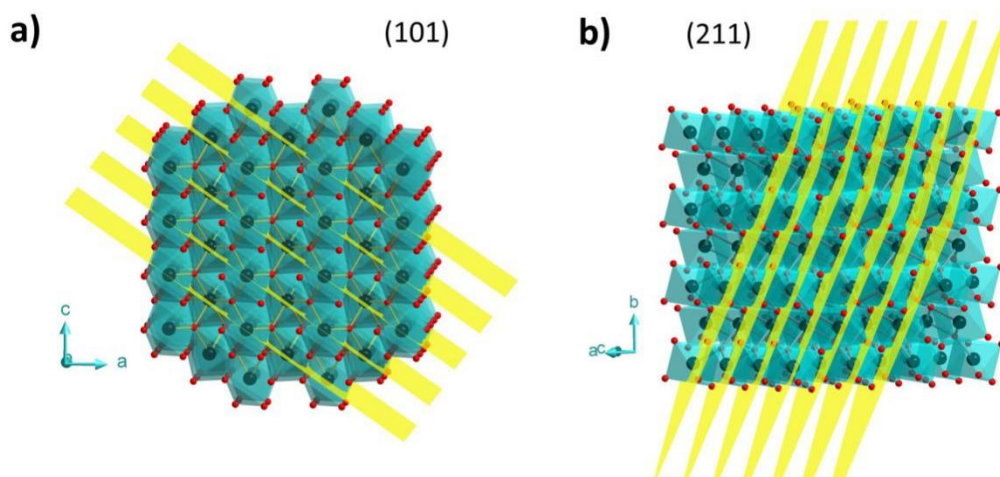
Figure S5. Crystal structure of RuO_2 viewed along different direction. The yellow planes represent the crystal facets of RuO_2. Related to Figure 1.
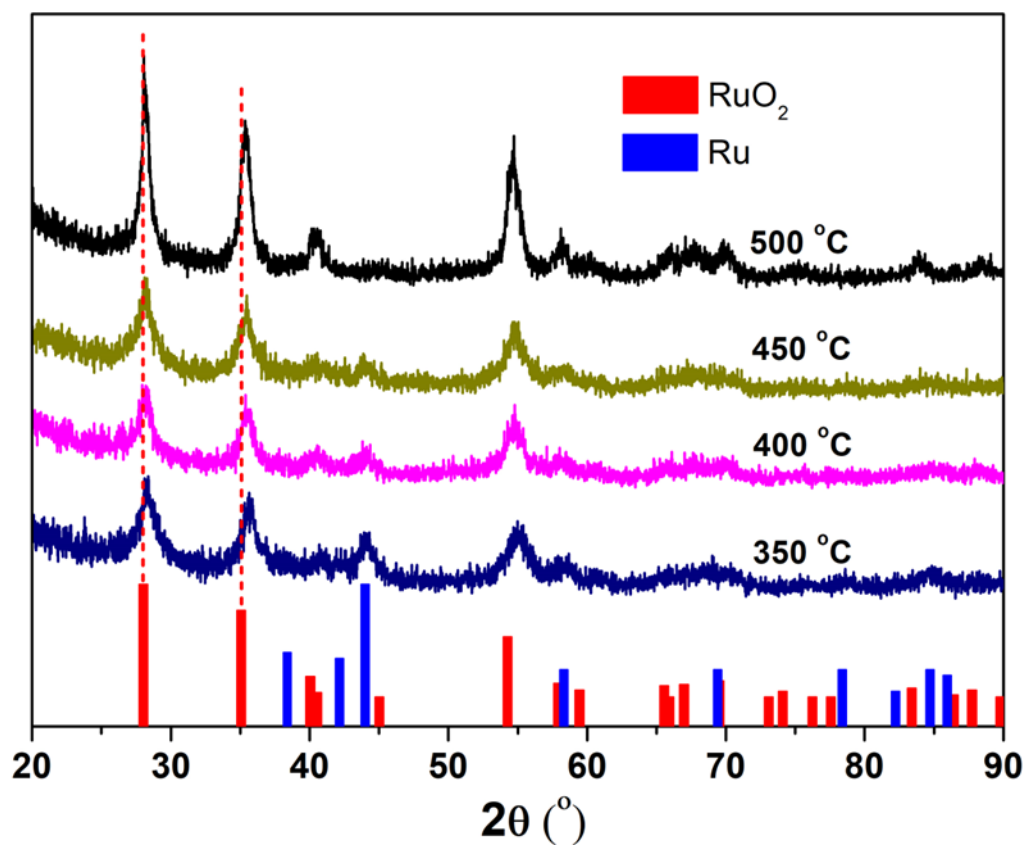
Figure S6. PXRD patterns of $Co_{0.11}Ru_{0.89}O_{2-\delta}$ annealed at different temperatures. Related to Figure 1.
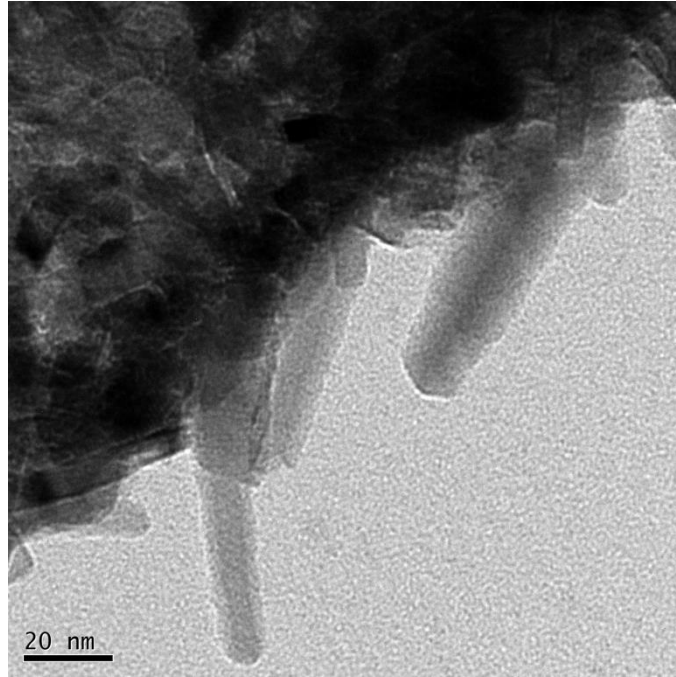
Figure S7. TEM image of $Co_{0.27}Ru_{0.73}O_{2-\delta}$ annealed at 350 ^{o}C . Related to Figure 2.
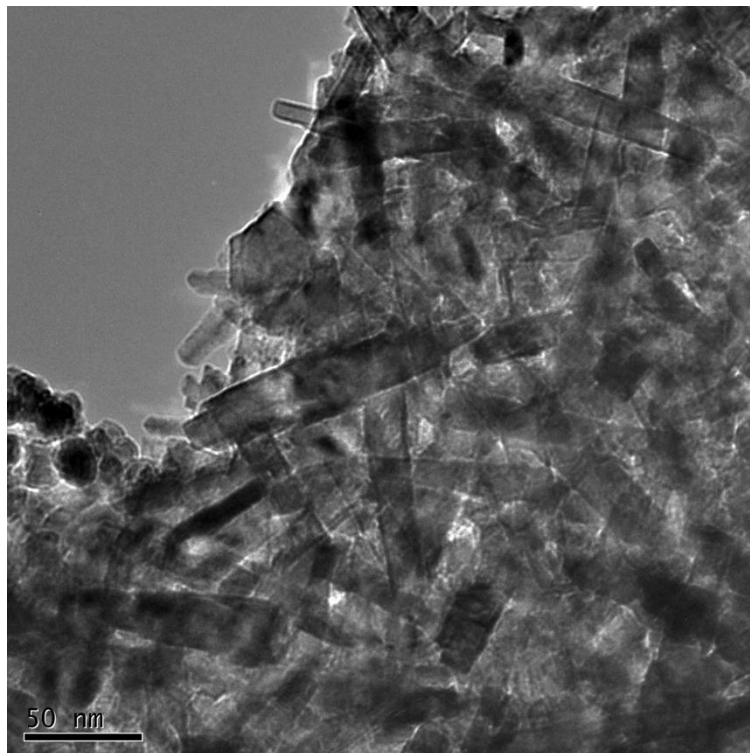
Figure S8. TEM image of $Co_{0.18}Ru_{0.82}O_{2-\delta}$ annealed at 350 ^{o}C . Related to Figure 2.
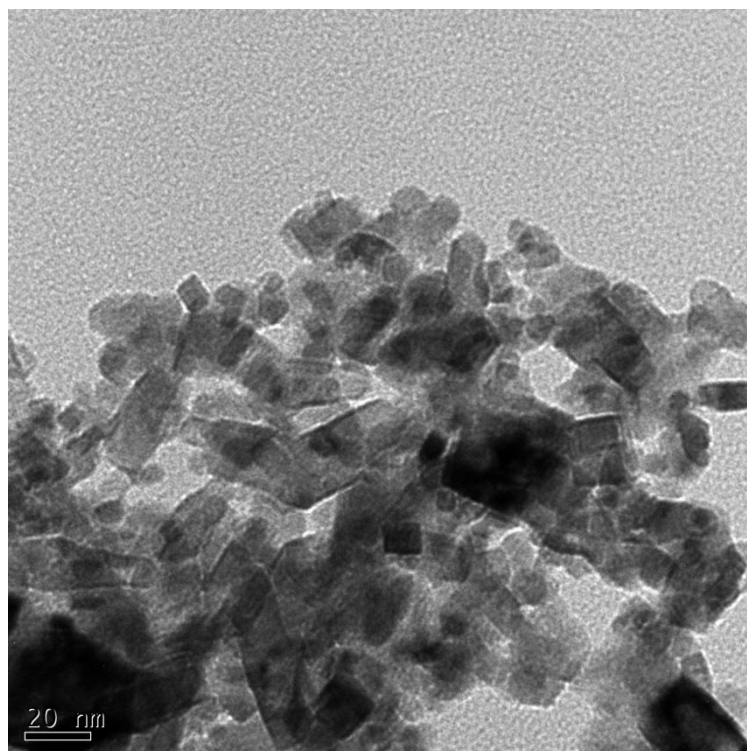
Figure S9. TEM image of $Co_{0.04}Ru_{0.96}O_{2-\delta}$ annealed at 350 ^{o}C . Related to Figure 2.
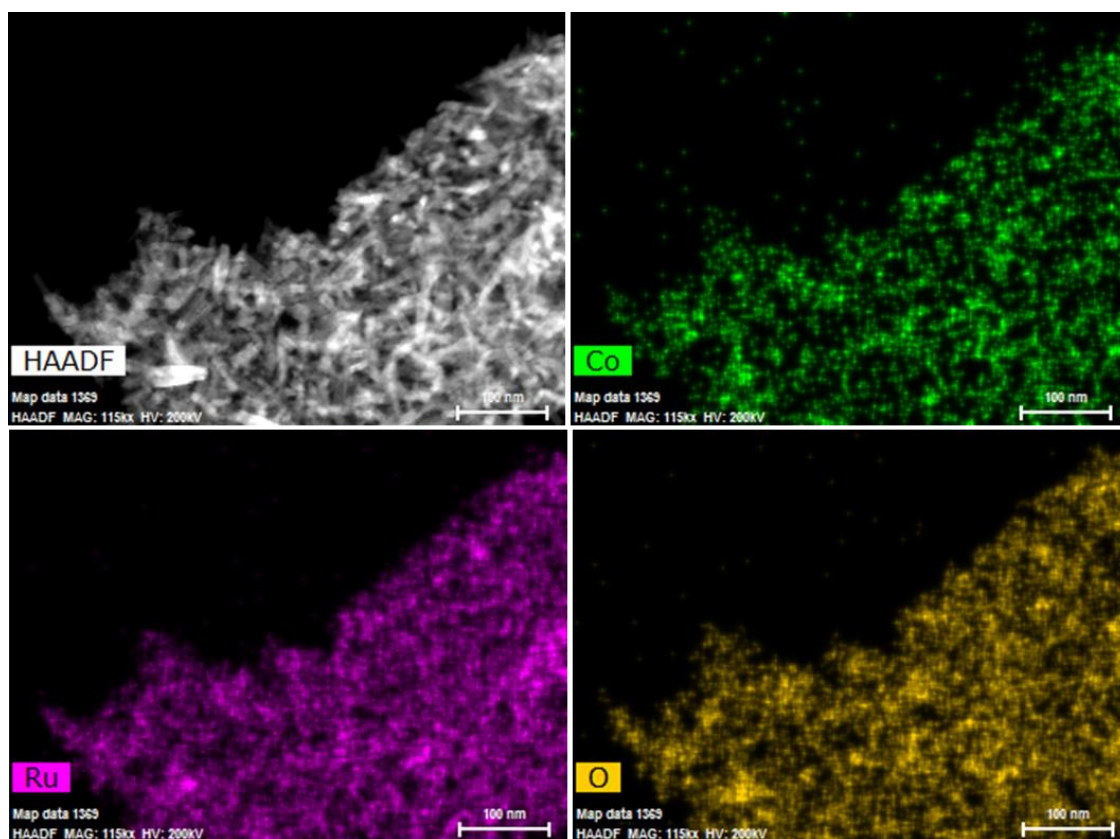
Figure S10. HAADF-STEM image and the corresponding element mapping images.

Related to Figure 2.
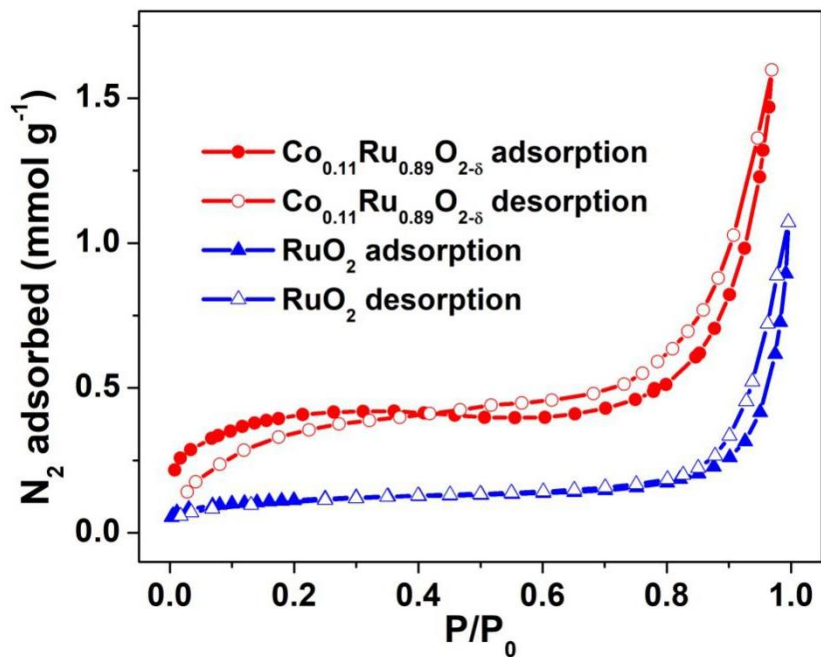
Figure S11. N_2 adsorption-desorption isotherms of $Co_{0.11}Ru_{0.89}O_{2-\delta}(350)$ and RuO_2 at 77 K. Related to Figure 2.
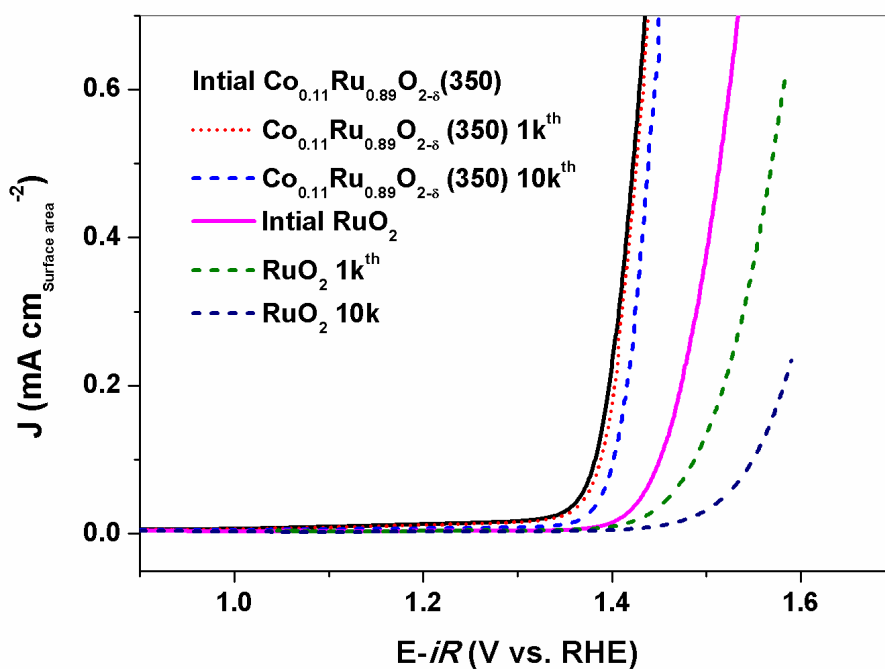
Figure S12. Intrinsic surface area based LSV curves of $Co_{0.11}Ru_{0.89}O_{2-\delta}$ (350) and commercial RuO_2 before and after CV cycling measurements. Related to Figure 3.
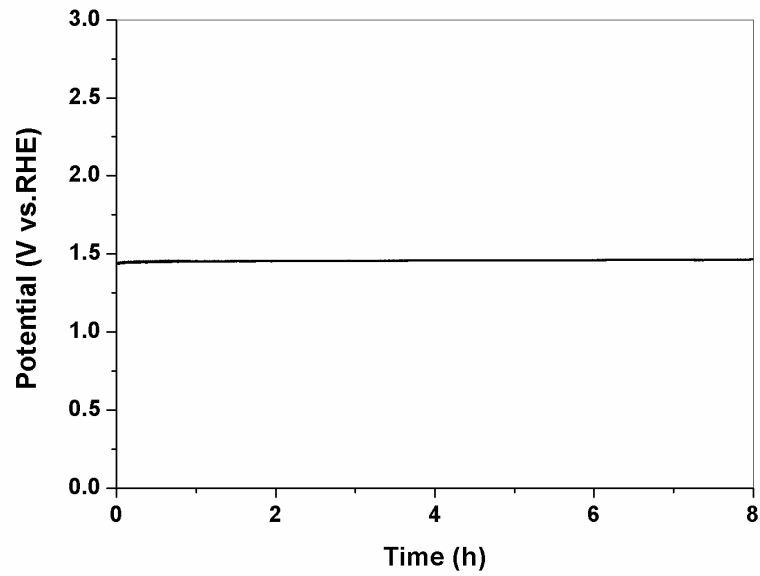
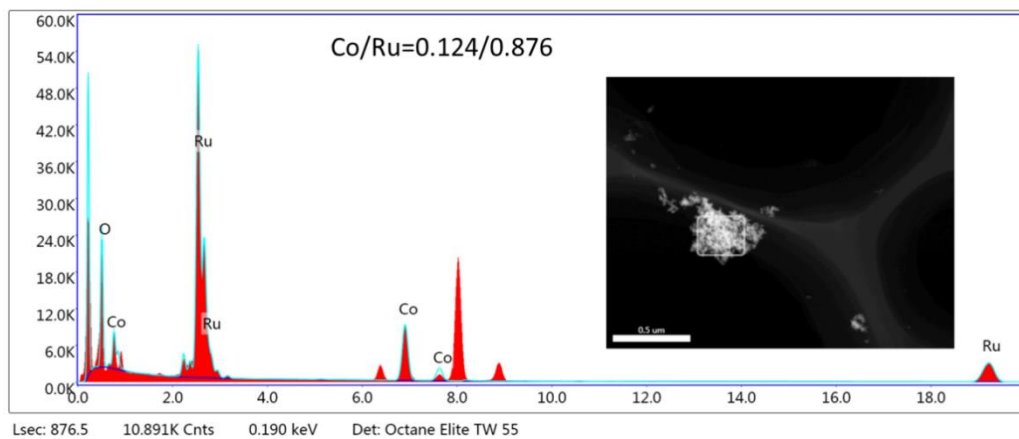Figure S13. Chronopotentiometry test of $Co_{0.11}Ru_{0.89}O_{2-\delta}$ (350) at the current density of 50 mA cm^{-2}. Related to Figure 3.

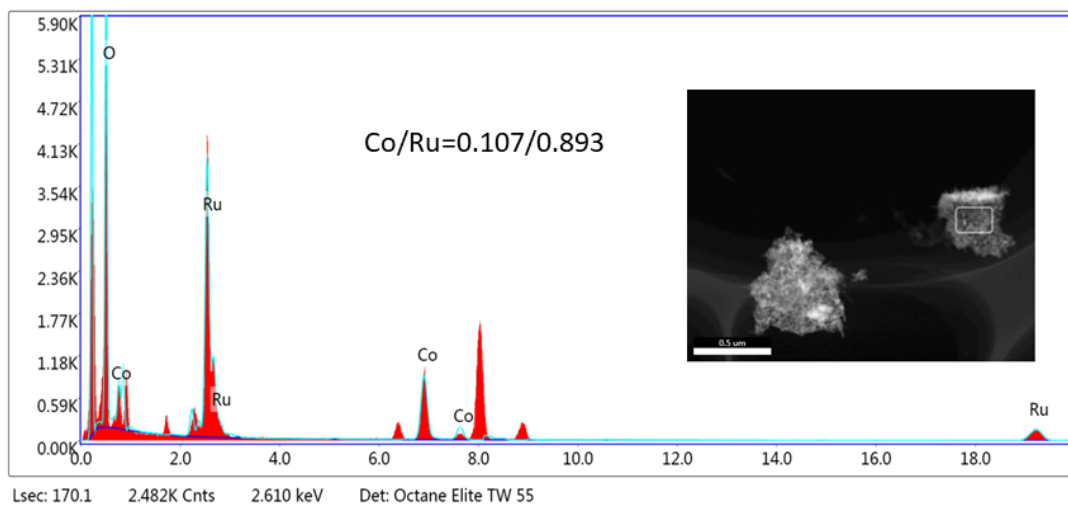Figure S14. TEM-EDS of $Co_{0.11}Ru_{0.89}O_{2-\delta}$ (350) before stability test. Related to Figure 3.

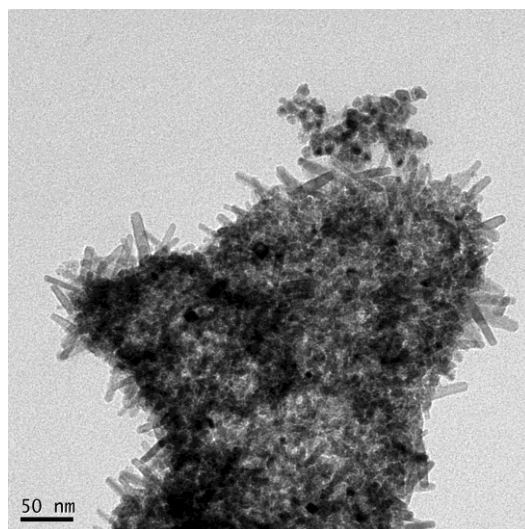Figure S15. TEM-EDS of $Co_{0.11}Ru_{0.89}O_{2-\delta}$ (350) after stability test. Related to Figure 3.

Figure S16. TEM image of f $Co_{0.11}Ru_{0.89}O_{2-\delta}$ (350) after stability test. Related to Figures 2 and 3.

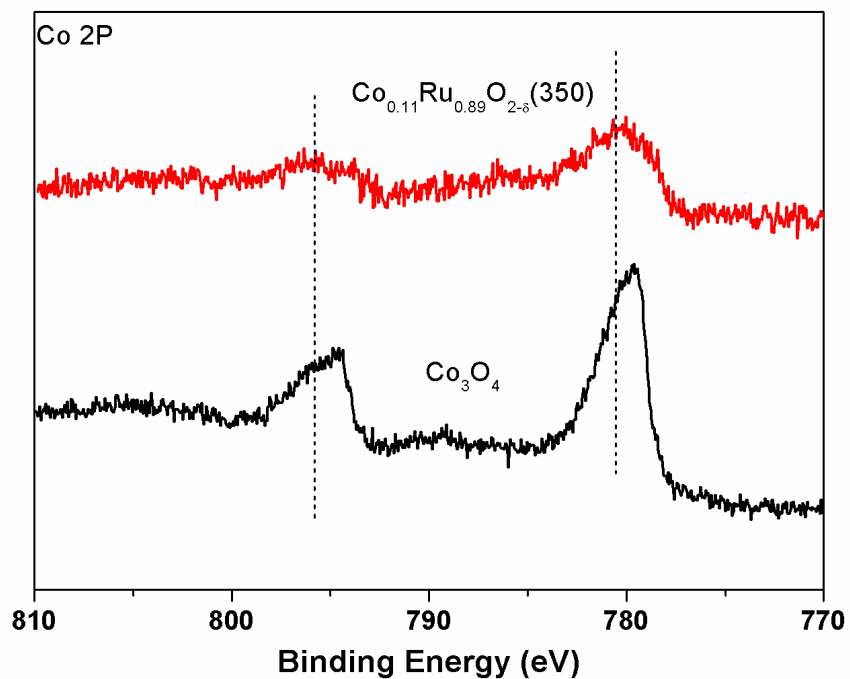Figure S17. Co 2P XPS profiles of $Co_{0.11}Ru_{0.89}O_{2-\delta}$ and Co_3O_4. Co_3O_4 was synthesized by annealing pure ZIF-67 at 350 ^oC. Related to Figure 4.
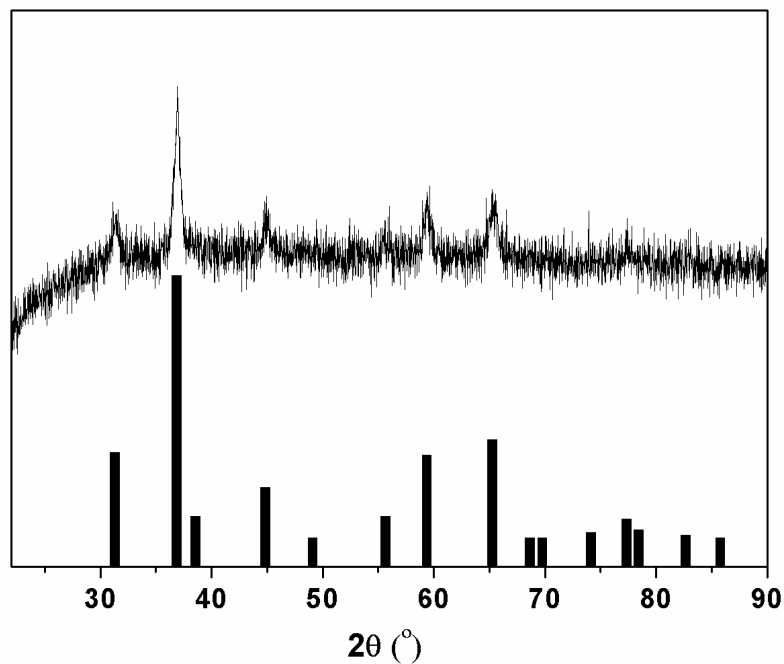

Figure S18. PXRD pattern of the product obtained from annealing pure ZIF-67. The reference patterns of Co_3O_4 were obtained from Jade 2004 (JCPDS No. 43-1003).

Related to Figure 4.

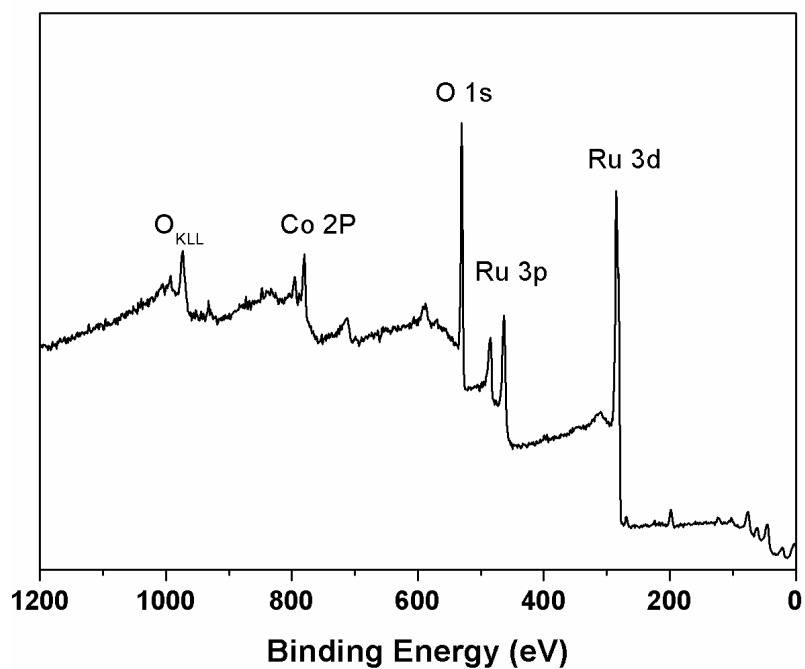Figure S19. The XPS wide-scan spectra of $Co_{0.11}Ru_{0.89}O_{2-\delta}(350)$. Related to Figure 4.
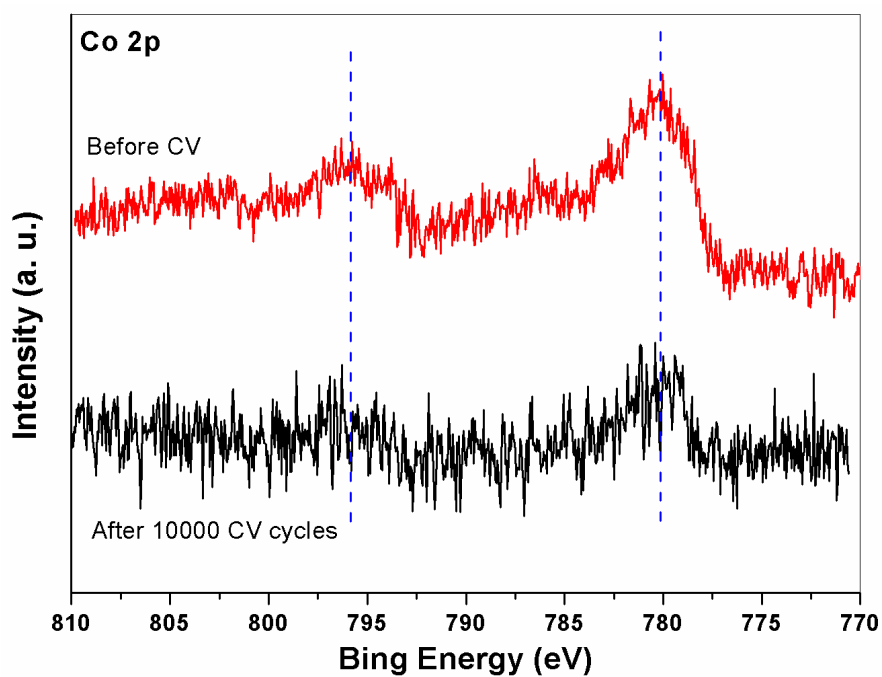

Figure S20. XPS spectra for Co of $Co_{0.11}Ru_{0.89}O_{2-\delta}$ (350) before and after 10000 CV cycles. Related to Figure 4.
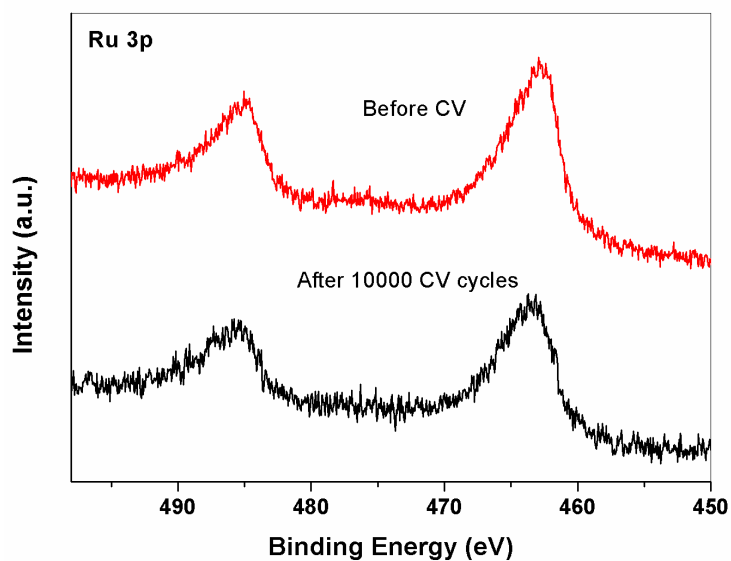
Figure S21. XPS spectra for Ru of $Co_{0.11}Ru_{0.89}O_{2-\delta}$ (350) before and after 10000 CV cycles. Related to Figure 4.
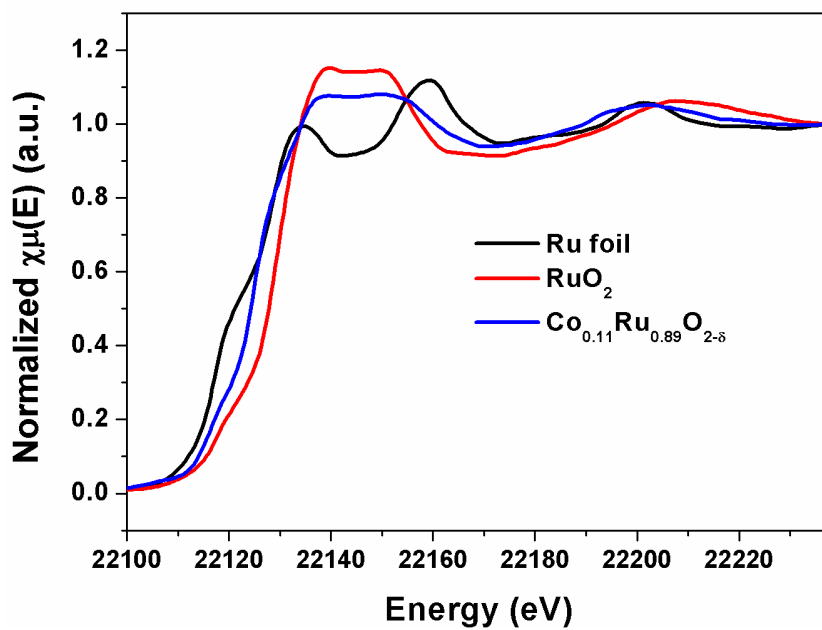

Figure S22. Normalized Ru K-edge XAS spectra of $Co_{0.11}Ru_{0.89}O_{2-\delta}$(350), RuO_2 and Ru foil. Related to Figure 4.
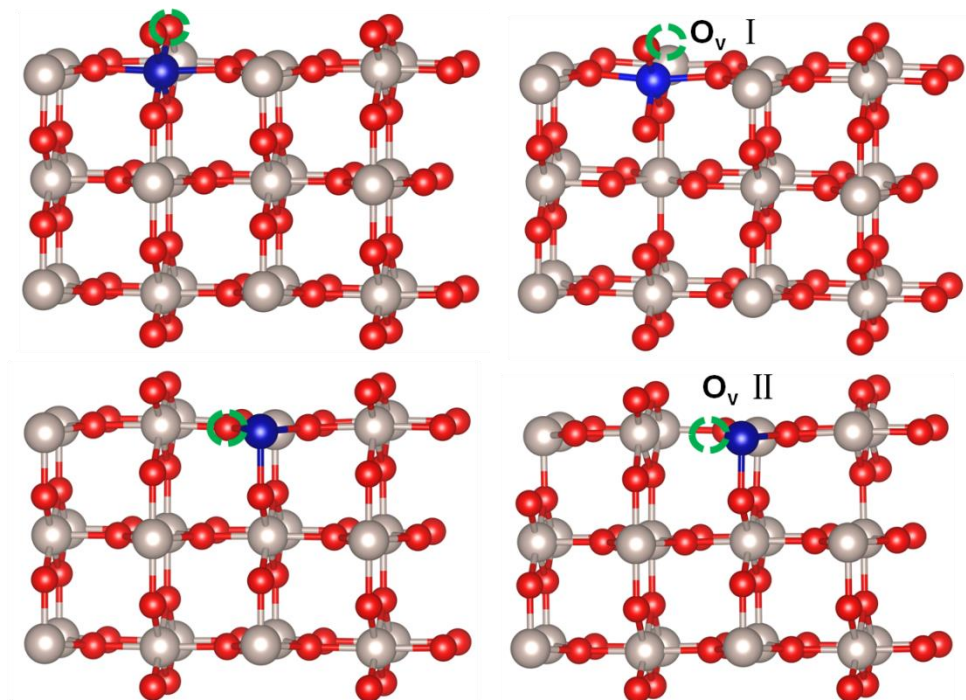
Figure S23. The formation of O vacancy for different Co doping sites. Related to Figure 5.
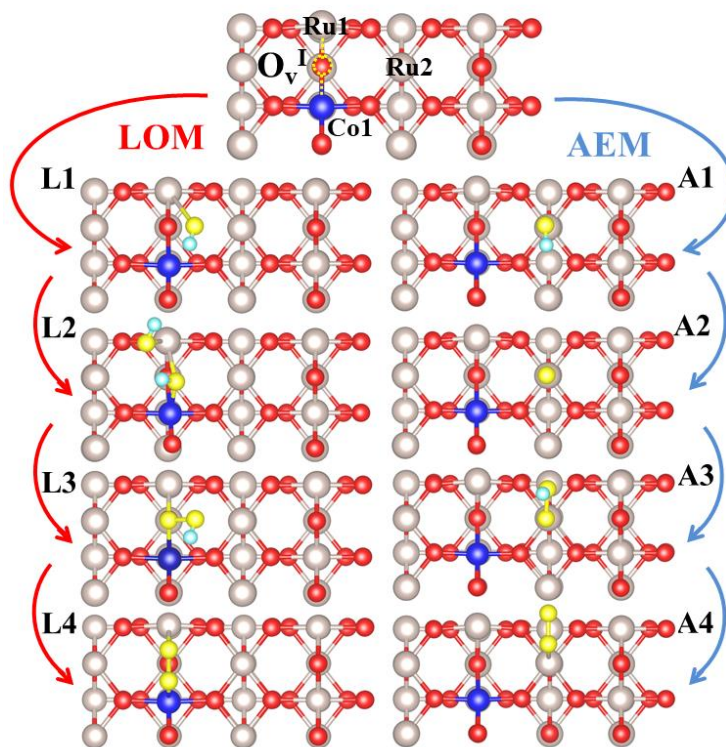
Figure S24. The intermediates along LOM and AEM processes. Related to Figure 5.
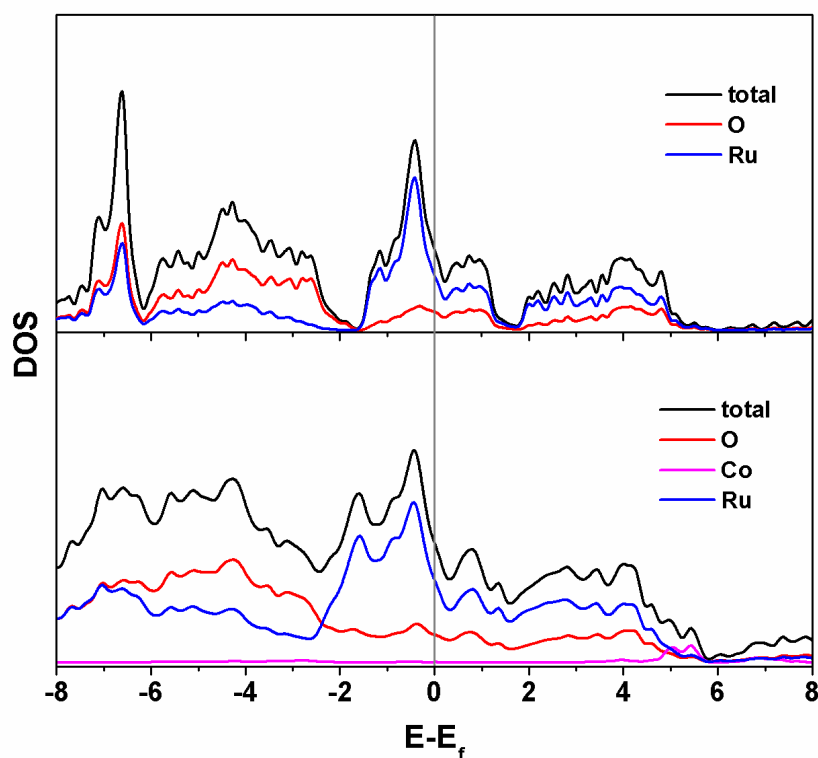
Figure S25. Calculated density of states (DOS) of bulk RuO_2 and Co-doped RuO_2. Related to Figure 5.

Table S1. The comparison of overpotentials of representative OER electrocatalysts in acidic media. Related to Figure 3.

Catalyst	substrate	Electrolyte	Overpotential at 10 mA cm^{-2} (mV)	Chronopotentiometry at specific current density	Ref.
Co-RuO_2	GCE	0.5 M H_2SO_4	169	50 h@10 mA cm^{-2}	**This work**
$Cr_{0.6}Ru_{0.4}O_2$(550)	GCE	0.5 M H_2SO_4	178	10 h @10 mA cm^{-2}	*Nat. Commun. 2019, 10:162*
Ba[Co-POM]	CP	1 M H_2SO_4	361	--	*Nat. Chem. 2018, 10, 24*
6H-IrO_2	GCE	0.5 M H_2SO_4	248	30 h @10 mA cm^{-2}	*Nat. Commun. 2018,9:5236*
IrCoNi PHNCs	GCE	0.1 M $HClO_4$	303	3.3 h@5 mA cm^{-2}	*Adv. Mater. 201, 729, 1703798,*
IrNiCu	GCE	0.1 M $HClO_4$	300	--	*ACS Nano. 2017,*

DNF					*11, 5500,*
Ir	GF	0.5 M H_2SO_4	290	10 h@10 mA cm^{-2}	*Nano Energy. 2017, 40, 27,*
$Ni_{0.5}Mn_{0.5}Sb_{1.7}Oy$	ATO	1 M H_2SO_4	~672	170 h@10 mA cm^{-2}	*Energy Environ. Sci. 2017, 10, 2103.*
$W_{0.57}Ir_{0.43}O_{3-\delta}$	FTO	1 M H_2SO_4	370	0.6 h@10 mA cm^{-2}	*Energy Environ. Sci. 2017, 10, 2432*
Co_3O_4	FTO	0.5 M H_2SO_4	570	12 h@10 mA cm^{-2}	*Chem. Mater. 2017, 29, 950*
$Y_2Ru_2O_{7-\delta}$	GCE	0.1 M $HClO_4$	270@1 mA cm^{-2}	8 h@1 mA cm^{-2}	*J. Am. Chem. Soc. 2017, 139, 12076*
IrO_2-RuO_2@Ru	GCE	0.5 M H_2SO_4	281	--	*J. Mater. Chem. A 2017, 5, 17221*
NiFeP	Free-standing	0.05 M H_2SO_4	540	12 h@10 mA cm^{-2}	*Adv. Mater. 2017, 29. 1606570*
IrNi NCs	GCE	0.1 M $HClO_4$	280	2 h@5 mA cm^{-2}	*Adv. Func. Mater. 2017. 27, 1700886*
Co-IrCu ONC	GCE	0.1 M $HClO_4$	290	--	*Adv. Func. Mater .2017, 27, 1604688*
IrO_x-Ir	GC plates	0.5 M H_2SO_4	290	100 h@2 mA cm^{-2}	*Angew. Chem. Int. Ed. 2016, 55, 752*
IrO_x/$SrIrO_3$	$SrTiO_3$	0.5 M H_2SO_4	270-290	30 h@10 mA cm^{-2}	*Science. 2016, 353, 1011*
$BaYIrO_6$	Au	0.1 M H_4ClO_4	~315	1 h@10 mA cm^{-2}	*Nat. Commun. 2016, 7, 12363*
Ir-Ni Oxide	Ti	0.1 M HClO4	~270	--	*J. Am. Chem. Soc. 2015, 137, 13031*
$IrNiO_x$	ATO	0.05 M H_2SO_4	~330	--	*Angew. Chem. Int. Ed. 2015, 54, 2975*
IrO_2	GCE	0.1 M H_4ClO_4	~430	--	*J. Electrochem. Soc. 1983, 130, 825*

Transparent Methods

Materials. All reagents are of analytical grade and used as received. The commercial RuO_2 and Nafion (5 wt% soluton) were purchased from Sigma-Aldrich.

Synthesis of ZIF-67. The ZIF-67 nanoparticles were synthesized via a procedure reported in literature. Cobalt nitrate hexahydrate (0.3 g) and 2-methylimidazole (0.66 g) were dissolved in methanol (11.3 g). The two solutions were then mixed and stirred at room temperature at 600 rpm for 24 h. The resulting purple precipitate was separated from the solution by centrifugation at 4000 rpm for 10 minutes and washed three times with methanol and dried overnight at 80 ^{o}C. The sample was further dried at 100 ^{o}C under vacuum for 12 h for future use.

Synthesis of Ru-ZIF-67. Typically, ZIF-67 (0.1 g) powder and desired amount of $RuCl_3 \cdot xH_2O$ were added into 15 mL tetrahydrofuran (THF) and allowed to stir for 24 h. The resulting precipitate was centrifuged and washed with 3 times with THF, then dried at 80 ^{o}C in air. To obtain different Ru content Ru-ZIF-67, the amount of $RuCl_3 \cdot xH_2O$ added was 0.2 g, 0.3 g, 0.4 g and 0.6 g respectively. For clearness, we denoted these samples as Ru-ZIF-67-A, Ru-ZIF-67-B, Ru-ZIF-67-C, and Ru-ZIF-67-D, respectively.

Synthesis of Co-doped RuO_2 nanorods. Co-doped RuO_2 powders were obtained by annealing Ru-ZIF-67 precursors in air at temperatures of 300~500 ^{o}C for 4 h. Typically, 20 mg of Ru-ZIF-67-C were placed in crucible and put into a muffle, and then annealed in air with a heating rate of 10 ^{o}C min^{-1} to 350 ^{o}C, and held at 350 ^{o}C for 4 h.

Characterizations. Powder X-ray diffractions (PXRD) characterization of the samples were performed on a D8-Advance Bruker AXS diffractometer with $Cu_{K\alpha}$ (λ=1.5418 Å)

radiation at a voltage of 40 kV and 40 mA. The sample morphologies were characterized using a field-emission scanning electron microscope (SEM) (Hitachi, S-4800). SEM specimens were prepared by depositing sample powders onto carbon adhesive tapes. Transmission electron microscopy (TEM) images and high-angle annular dark-field scanning transmission electron microscopy (HAADF-STEM) images were carefully recorded on Talos F200X and JEM-ARM200F. The chemical composition and bonding states were measured by X-ray photoelectron spectroscopy (XPS) using a Kratos AXIS ULTRA[DLD] instrument with a monochromic Al-Kα X-ray source (hν=1496.6 eV). The power was 120 W and the X-ray spot size was set to 700×300 μm. The pass energy of the XPS analyzer was set as 20 eV. The base pressure of the analysis chamber was better than $5×10^{-9}$ Torr. The nitrogen adsorption-desorption isotherm was measured on ASAP 2020M apparatus at 77 K. Before the measurements, the samples were outgassed under vacuum at 160 ^{o}C for 12 hours. Raman spectra were recorded on a Renishaw inVia Reflex spectrometer. Inductively coupled plasma-mass spectroscopy (ICP-MS) measurements were carried on NexION 300 (Perkin-Elmer).

Electrochemical measurements. In a typical procedure, 4 mg of Co-RuO$_2$ powder was added to 1 mL of water/ethanol (3:1, v/v) containing 15 μL Nafion aqueous solution (5%, Sigma-Aldrich), and dispersed by sonication under shaking for 30 min to generate a homogeneous black ink. 5 μL of the prepared catalyst ink was drop-cast on a glassy carbon electrode (Geometric area: 0.07065 cm^2) and dried at room temperature to form a thin film working electrode. A three-electrode system, contained a glassy carbon working electrode, a counter electrode made of platinum wire (diameter: 0.5 nm), and a saturated Hg/Hg$_2$SO$_4$

reference electrode, were used to measure the electrochemical properties. All measurements were performed in 0.5 M H_2SO_4 acidic solution. The Hg/Hg_2SO_4 reference electrode was calibrated with a Pt wire electrode in H_2-satured 0.5 M H_2SO_4 solution. The results showed that the potential difference between the Hg/Hg_2SO_4 reference electrode and reversible hydrogen electrode was 0.645 V. Cyclic voltammograms (CVs) tests were collected at a scan rate of 100 mV s^{-1} typically between 1.2 and 1.6 V. Chronopotentiometric measurements were carried out by applying a constant current of 10 mA cm^{-2} for up to 50 h. Electrochemical impedance spectroscopy (EIS) were performed at 1.4 V. The EIS results were presented in the form of Nyquist plot and fitted using ZView software with a representative equivalent electrical circuit. We carried out iR correction according to the literatures reported.[Zheng et al. 2017; Li et al. 2017] The potential was manually corrected using Ohm's law: $E=E_{app}-iR_s*0.85$, where Rs (solution resistance) is determined to be 9 Ω by EIS (Figure 3c).

Calculation details

All DFT calculations are carried out by using the Vienna ab-initio Simulation Package (VASP) [Kresse, et al. 1996] to optimize geometry structures and energies. The exchange–correlation functional is performed within the generalized gradient approximation proposed by Perdew–Burke–Ernzerh (GGA-PBE).[Perdew, et al. 1996; Perdew, et al. 1992;] The core electrons is described by the Projector Augmented Wave (PAW) potential,[Blochl, et al. 1994] and the cut-off kinetic energies for the plane waves are set to 500 eV.[Kresse, et al. 1994] The convergence criteria of energy and force on each atom after relaxation are less than 10^{-4} eV

and 0.02 eV/A˚, respectively. The RuO$_2$(110) is built with 2*2 supercell with fixing two bottom layers in the geometry optimization. The Brillouin zone is sampled by Gamma point [Hendrik, et al. 1976] and a vacuum distance of 15 Å along z direction was set to ensure sufficient vaccum on surface. The Thermal and zero point energy (ZPE) corrections are further calculated by DFT-D3 to obtain the Gibbs free energy (ΔG), which is determined following ΔG = ΔE + ΔEZPE − TΔS, according to the standard hydrogen electrode (SHE) model proposed by Nørskov et al.[Peterson, et al. 2010] Grimme's DFT-D3 scheme are expected to provide dispersion correction in van der Waals (vdW) interactions.[Grimme, et al. 2010; Grimme, et al. 2011] ΔE, ΔEZPE and ΔS are the electronic total energy differences, the differences in the zero point energy and the change of entropy, respectively. T is the temperature set to 298.15 K.

Free energy calculations: The Gibbs free energy changes are calculated by the following equations (1) to (4) for AEM while those for LOM are calculated by the equations (5) to (8) [Rossmeisl, et al. 2005].

$$\Delta G_1 = \Delta G_{O*} - \Delta G_{OH*} - eU + \Delta G_{H+} \ (pH) \tag{1}$$

$$\Delta G_2 = \Delta G_{OOH*} - \Delta G_{O*} - eU + \Delta G_{H+} \ (pH) \tag{2}$$

$$\Delta G_3 = \Delta G_{OO*} - \Delta G_{OOH*} - eU + \Delta G_{H+} \ (pH) \tag{3}$$

$$\Delta G_4 = 4.92eV + \Delta G_{OH*} - \Delta G_{OO*} - eU + \Delta G_{H+} \ (pH) \tag{4}$$

$$\Delta G_1 = \Delta G_{[Ov-OH]*} - \Delta G_{[Ov-OO]*} - eU + \Delta G_{H+} \ (pH) \tag{5}$$

$$\Delta G_2 = \Delta G_{[OH+Ov-OH)]*} - \Delta G_{[Ov-OOH]*} - eU + \Delta G_{H+} \ (pH) \tag{6}$$

$$\Delta G_3 = \Delta G_{[Ov-OOH)]*} - \Delta G_{[OH+Ov-OH)]*} - eU + \Delta G_{H+} \ (pH) \tag{7}$$

$$\Delta G_4 = 4.92\,\text{eV} + \Delta G_{[Ov\text{-}OO]^*} - \Delta G_{[Ov\text{-}OOH)]^*} - eU + \Delta G_{H_+}\,(p\text{H}) \qquad\qquad (8)$$

where U is the potential determined against by normal hydrogen electrode (NHE) at standard condition (T = 298.15 K, P = 1 bar, pH = 0)[Nørskov et al. 2004]. The free energy changes of the protons relative to the above-specified electrode at non-zero pH is represented by Nernst equation as $\Delta G_{H_+}\,(p\text{H}) = -k_B T\,\ln(10) \times p\text{H}$. The Gibbs free energy differences of these intermediates include zero-point energy (ZPE) and entropy corrections according to $\Delta G = \Delta E + \Delta ZPE - T\Delta S$, where the energy differences ΔE are calculated with respect to H_2O and H_2 (at U = 0 and pH = 0). The theoretical overpotential is defined as the lowest potential at which all reaction steps are thermodynamically downhill.[Man, et al. 2011; Doyle, et al. 2015]

References

Blochl, P. E. (1994). Projector augmented-ware method. Phys. Rev. B. *50*, 27.

Doyle, A. D., Montoya, J. H., Vojvodic, A. (2015) Improving oxygen electrochemistry through nanoscopic confinement. ChemCatChem *7*, 738.

Grimme, S., Antony, J., Ehrlich, S., Krieg, H. (2010). A consistent and accurate ab initio parametrization of density functional dispersion correction (DFT-D) for the 94 elements H-Pu. J. Chem. Phys. *132*, 154104.

Grimme, S., Ehrlich, S., Goerigk, L. (2011). Effect of the Damping Function in Dispersion Corrected Density Functional Theory. J. Comput. Chem. *32*, 1456.

Hendrik, J., Ma, J. (1976). Special points for Brillouin-zone integratiionns. Phys Rev B. *13*, 5.

Kresse, G., Furthmuller, J. (1996). Efficient iterative schemes for *ab* initio total-energy calculations using a plane-wave basis set. Phys. Rev. B *54*, 11169-11186.

Li, Y., Cui, F., Ross, M.B., Kim, D., Sun, Y., Yang, P. (2017). Structure-sensitive CO_2 electroreduction to hydrocarbons on ultrathin 5-fold twinned copper nanowires. Nano Lett. *17*, 1312-1317.

Man I. C. et al. (2011). Universality in oxygen evolution electrocatalysis on oxide surfaces. ChemCatChem, *3*, 1159.

Nørskov J. K. et al. (2004). Origin of the overpotential for oxygen reduction at a fuel-cell cathode. J. Phys.Chem. B *108*, 17886.

Perdew, J.P., Burke, K., Ernzerhof, M. (1996). Generalized gradient approximation made simple. Phys. Rev. Lett. *77*, 3865.

Perdew J.P., Wang Y. (1992). Pair-distribution function and its coupling-constant average for the spin-polarized electron gas. Phys. Rev. B: Condens Matter. *46*, 12947.

Peterson, A. A., Abild-Pedersen, F., Studt, F., Rossmeisl, J., Norskov, J. K. (2010). How copper catalyzes the electroreduction of carbon dioxide into hydrocarbon fuels. Energy Environ. Sci. *3*, 1311.

Rossmeisl, J., Logadottir, A., Nørskov J.K. (2005). Electrolysis of water on (oxidized) metal surfaces, Chem. Phys. *319*, 178.

Zheng, X., et al (2017). Sulfur-modulated tin sites enable highly selective electrochemical reduction of CO_2 to format. Joule, *1*, 794–805.